ELSEVIER

Sensors and Actuators 72 (1999) 49–70

SENSORS AND ACTUATORS A PHYSICAL

Phenomenological model for gas-damping of micromechanical structures

Dennis S. Greywall [a,*], Paul A. Busch [a], James A. Walker [b]

[a] *Bell Laboratories, Lucent Technologies, Murray Hill, NJ 07974, USA*
[b] *Bell Laboratories, Lucent Technologies, Holmdel, NJ 07733, USA*

Received 11 December 1997; revised 11 May 1998; accepted 12 July 1998

Abstract

Simple analytic expressions are presented which describe the gas-damping of squeeze-type micromechanical structures and which set design criteria for optimum response. The model is shown to accurately represent experimental data obtained for a device intended to function as an optical modulator with fiber-to-the-home applications.

Keywords: Gas-damping; Frequency response; Square-wave response

1. Introduction

Operating frequencies of micromechanical devices can extend into the MHz regime where damping to prevent ringing can become a serious issue. In this paper, we propose a very simple model which incorporates the essential elements of an actual gas-damped device and for which the mechanical response can be determined analytically. The derived expressions, with empirically determined parameters, are demonstrated to accurately describe the behavior of a drumhead-type optical modulator. This device consists mechanically of a tensioned diaphragm, with a number of small holes, which forms the lid over a small cylindrical volume. The phenomenological model represents a new approach to the very complicated damping problem [1–13].

2. Model

The model device shown in Fig. 1 consists of a piston of mass m and cross-sectional area a which is supported within a cylinder by a mechanical spring with spring constant k. The piston has small holes to provide an escape for the gas trapped in the cylinder and at equilibrium, sits a distance h above the bottom of the cylinder. Because the assembly is located in a large volume, the gas pressure above the piston remains at the ambient gas pressure P_o, independent of the piston's position and the instantaneous pressure P in the cylinder.

The linearized equation of motion for the sinusoidally driven resonator is

$$m\ddot{x} = -kx - (P - P_o)a - \Gamma\dot{x} + F_o e^{i\omega t}, \tag{1}$$

where x is the piston's displacement from equilibrium and Γ is the ordinary damping constant associated with the piston's velocity. The solution of Eq. (1) is represented by the expressions

$$x = Ae^{i(\omega t - \phi_1)} \tag{2}$$

and

$$P - P_o = Be^{i(\omega t - \phi_2)}, \tag{3}$$

where in general, $\phi_1 \neq \phi_2$.

The amplitudes A and B are given by analytic functions if it is assumed that the piston displacements are small compared to h, and if the simplification is made that the rate of gas flow through the holes in the piston is proportional to the instantaneous pressure difference $P - P_o$, that is,

$$\dot{n} = -\xi(P - P_o). \tag{4}$$

Although the conductance ξ is treated as a constant for a particular device, it is, in general, a very complicated function depending on many parameters, including: the number, size, and physical arrangement of the holes in the

* Corresponding author. Tel.: +1-908-582-6144; Fax: +1-908-582-3260; E-mail: dsgreywall@lucent.com

0924-4247/99/$ - see front matter
PII: S0924-4247(98)00203-9

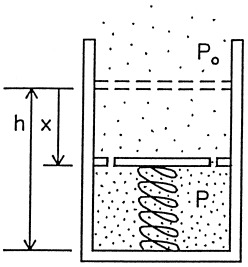

Fig. 1. Model device.

piston; the gap size h; the type of gas used; and the mean free path of the gas molecules.

A straightforward analysis shows that the displacement amplitude is determined by the relation

$$A\left[\omega_o^2+\frac{\omega_g^2}{1+(\omega\tau)^{-2}}-\omega^2+i\left(\frac{\omega_g}{\omega\tau}\cdot\frac{1}{1+(\omega\tau)^{-2}}+\frac{\omega\Gamma}{m}\right)\right]=\frac{F_o}{m}e^{i\phi_1}, \tag{5}$$

where

$$\omega_o^2\equiv\frac{k}{m}, \tag{6}$$

$$\omega_g^2\equiv\frac{aP_o/h}{m}, \tag{7}$$

and

$$\frac{1}{\tau}\equiv\frac{P_o\xi}{n_0} \tag{8}$$

$$=\frac{RT}{ah}\xi. \tag{9}$$

The parameter ω_o is the resonant frequency of the piston in the limit $P_o\to 0$; ω_g is the resonant frequency of the piston in the limit that $k\to 0$, and τ is the characteristic time associated with the decay of pressure in the fixed volume ah.

The imaginary term on the left side of Eq. (5) has two components: one due to the usual damping coefficient Γ, the second due to the out-of-phase component of the cylinder pressure. To simplify the discussion, it will be assumed that the term in Γ is small enough to be neglected. The expressions for the displacement's amplitude and phase are then

$$A=\frac{F_o/m\omega_o^2}{\sqrt{\left(1+\frac{\omega_g^2/\omega_o^2}{1+(\omega\tau)^{-2}}-\frac{\omega^2}{\omega_o^2}\right)^2+\left(\frac{\omega_g^2/\omega_o^2}{\omega\tau}\cdot\frac{1}{1+(\omega\tau)^{-2}}\right)^2}} \tag{10}$$

and

$$\tan\phi_1=\frac{\omega_g^2/\omega\tau}{\left(\omega_o^2-\omega^2\right)\left(1+(\omega\tau)^{-2}\right)+\omega_g^2}. \tag{11}$$

It can also be shown that the pressure response is given by

$$B=\frac{P_oF_o/hm\omega_o^2}{\sqrt{2\left(1-\frac{\omega^2}{\omega_o^2}\right)\frac{\omega_g^2}{\omega_o^2}+\left(1-\frac{\omega^2}{\omega_o^2}\right)^2(1+(\omega\tau)^{-2})+\frac{\omega_g^4}{\omega_o^4}}} \tag{12}$$

and

$$\tan\phi_2=\frac{1}{\omega\tau}\cdot\frac{\left(\omega^2-\omega_o^2\right)}{\left(\omega_o^2+\omega_g^2-\omega^2\right)}. \tag{13}$$

Eqs. (10)–(13) are the framework of the model.

3. Special drive frequencies

3.1. $\omega = 0$

If there is at least one hole in the piston, then $1/\tau\neq 0$ and Eqs. (10) and (12) yield in the limit of zero frequency, $A\to F_o/m\omega_o^2=F_o/k$ and $B\to 0$. The motion of the piston is now slow enough to allow the cylinder pressure to remain at P_o. The restoring force is then due only to the mechanical spring.

3.2. $\omega\to\infty$

In this limit, $A\to 0$ and $B\to 0$. Now the drive frequency is so large that the piston, because of its inertia, cannot respond to the oscillatory force and remains stationary. Consequently, the cylinder pressure again remains at P_o.

3.3. $\omega\tau\ll 1$

If one thinks of the drive frequency as being fixed, this case corresponds to a very small value of τ and so, to a piston with a very high porosity. Eq. (10) simplifies to

$$A=\frac{F_o/m\omega_o^2}{\sqrt{\left(\frac{\omega_o^2-\omega^2}{\omega_o^2}\right)^2+\left(\frac{\omega_g^2}{\omega_o^2}\omega\tau\right)^2}}, \tag{14}$$

which has the form of the usual resonance equation. The resonance peak is centered at $\omega=\omega_o$ and has a width determined by the quality factor Q, with

$$Q=\frac{\omega_o}{\tau\omega_g^2}. \tag{15}$$

Because the piston is very porous, the gas cannot contribute to the piston's restoring force and shift the resonant frequency. It is, however, responsible for the damping.

3.4. $\omega\tau \gg 1$

This is the opposite case of a piston with a very low porosity and with the trapped gas making its maximum contribution to the total restoring force. Eq. (10) becomes

$$A = \frac{F_o/m\omega_o^2}{\sqrt{\left(\frac{\omega_o^2+\omega_g^2-\omega^2}{\omega_o^2}\right)^2+\left(\frac{\omega_g^2}{\omega_o^2}\frac{1}{\omega\tau}\right)^2}}, \quad (16)$$

which has a peak at

$$\omega = \sqrt{\omega_o^2+\omega_g^2}. \quad (17)$$

The effective quality factor

$$Q = \frac{\omega_o\omega^2\tau}{\omega_g^2} \quad (18)$$

now depends on the square of the drive frequency.

If $\omega_g \preceq \omega_o$, as is typically the case (Section 4), and ω is small compared to ω_o, but not so small as to violate the condition $\omega\tau \gg 1$, then, Eq. (16) simplifies to

$$A \approx \frac{F_o}{m\omega_o^2}\cdot\frac{1}{1+\omega_g^2/\omega_o^2}. \quad (19)$$

So when ω_g is comparable to ω_o, the low frequency amplitude falls significantly below the low frequency limit of $F_o/m\omega_o^2$. This behavior is very different from the usual high-Q resonance behavior (e.g., Section 3.3), where the low frequency amplitude remains roughly at the limiting value. A rapid decrease in the amplitude of the frequency response at low frequencies followed at higher frequencies by a sharp resonance peak immediately indicates a small porosity.

3.5. $\omega = \omega_o$

At this special frequency, Eq. (12) for the pressure amplitude can be written as

$$B = \frac{P_o F_o}{hm\omega_o^2}\cdot\frac{\omega_o^2}{\omega_g^2}, \quad (20)$$

which is independent of the porosity (i.e., τ) of the piston. On the other hand, a very porous piston exhibits a resonance at ω_o and undergoes very large physical displacements (Section 3.3). So as the porosity increases and gas passes more easily through the piston, the physical amplitude of the piston's motion grows to a level just sufficient to maintain constant the amplitude of the pressure swings. Note too that the pressure is in phase with the drive, i.e., $\phi_2 \equiv 0$ (Eq. (13)).

3.6. $\omega = \sqrt{\omega_o^2+\omega_g^2}$

As shown above in Section 3.4, resonance occurs at this frequency when the piston has a very low porosity, i.e., when $\omega\tau \gg 1$. But independent of porosity and so, independent of whether or not there is resonance behavior, the pressure at this frequency lags the drive according to Eq. (13) by precisely 90°.

3.7. $\omega = \omega_o\sqrt{1+\omega_g^2/2\omega_o^2}$

At this frequency, Eq. (10) for the displacement simplifies to

$$A = \frac{F_o}{m\omega_o^2}\cdot\frac{2\omega_o^2}{\omega_g^2}. \quad (21)$$

Now it is the piston's amplitude which is independent of the porosity.

Various types of plots will be presented in the following sections which explicitly demonstrate all of these special cases.

4. Magnitude of ω_g

Typically, the characteristic frequency $f_o = \omega_o/2\pi$ of a micromechanical structure lies in the broad frequency range between low kHz and low MHz. In this section, it is shown that the gas frequency $f_g = \omega_g/2\pi$, at atmospheric

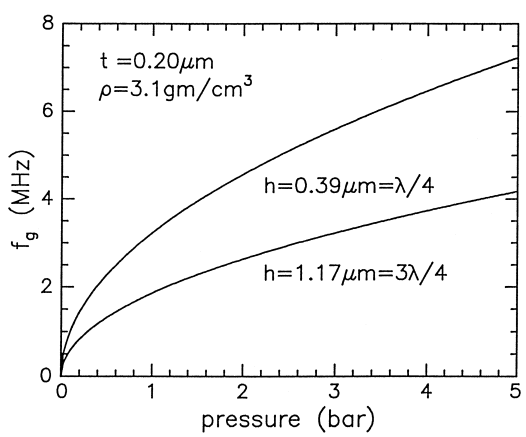

Fig. 2. Gas frequency f_g vs. pressure determined using Eq. (24). The two curves correspond to piston-cylinder assemblies which differ only in gap spacing h.

pressure, is typically of the order of MHz and so, generally greater than f_o.

The gas frequency was defined by Eq. (7), i.e.,

$$\omega_g = \sqrt{\frac{aP_o}{hm}} \,. \tag{22}$$

If the piston has uniform thickness t, then,

$$m = at\rho, \tag{23}$$

where ρ is the density, and so,

$$f_g = \frac{1}{2\pi}\sqrt{\frac{P_o}{ht\rho}} \,. \tag{24}$$

In anticipation of the experimental results to be discussed in Section 11, we take as an example a piston made of silicon nitride ($\rho = 3.1$ g/cm^3) with a thickness of 0.2 μm. The gap spacing is either 0.39 or 1.17 μm. These gaps correspond, respectively, to $\lambda/4$ or $3\lambda/4$ with $\lambda =$ 1.56 μm, and are optimum spacings for the devices to function as optical modulators. Fig. 2 shows f_g for the two spacings plotted as a function of pressure.

It will be shown in Section 10, that it is desirable to have $f_g \geq 2f_o$. So, for example, if one requires f_o to be 3 MHz, then f_g should be 6 MHz. The curve for $h = 0.39$ μm in Fig. 2 shows that the ambient gas pressure will need to be of the order of 3 bars. Because f_g and f_o have the same mass dependence, f_g/f_o is independent of m.

5. Amplitude and pressure plots with $\omega_g/\omega_o = 2$

Many of the essential physical implications of the model are depicted in Fig. 3. This three-dimensional plot shows A (Eq. (10)) vs. ω and $1/\tau$, in dimensionless units, for

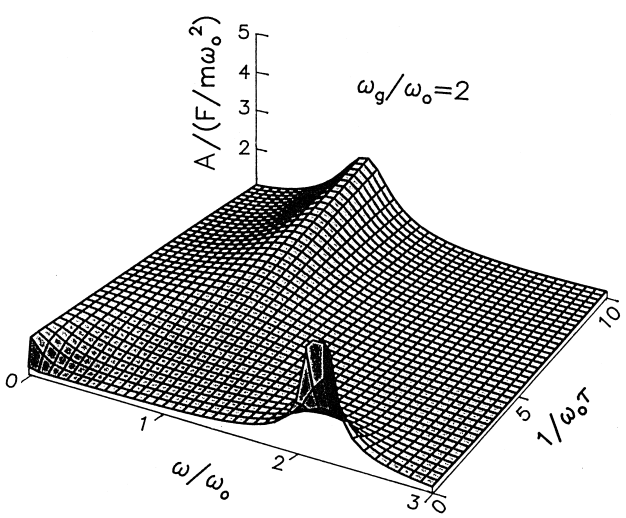

Fig. 3. Displacement amplitude plotted vs. drive frequency and 'piston porosity', all in dimensionless units. The reduced gas frequency is fixed at 2.

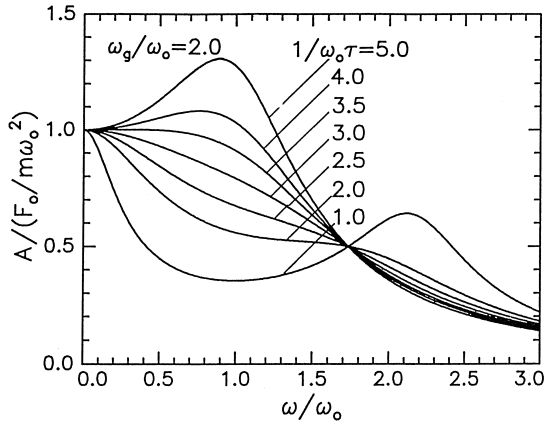

Fig. 4. Displacement amplitude as a function of drive frequency. Curves are shown for ω_g/ω_o fixed at 2, and for various values of $1/\omega_o\tau$. The node occurs at $\omega/\omega_o = \sqrt{1+\omega_g^2/\omega_o^2} = \sqrt{3}$.

ω_g/ω_o fixed at 2.0. Remember that $1/\tau$ is a measure of the piston's porosity.

For low porosities (i.e., $1/\omega_o\tau \approx 0$), there is a sharp resonance peak at $\omega/\omega_o \approx \sqrt{1+\omega_g^2/\omega_o^2} = \sqrt{5}$ and at low frequencies, a reduced response amplitude much smaller than unity. As the porosity increases, this behavior evolves, with the peak amplitude first decreasing and then reemerging near $\omega/\omega_o = 1$. For $1/\omega_o\tau \geq 10$, the frequency response shows more-ordinary behavior with the reduced amplitude increasing monotonically from unity on the low frequency side of the peak. These two extreme cases for $1/\tau$ were discussed more quantitatively in Section 3.

In the transitional region, the calculated response (with ω_g/ω_o fixed at 2) does not exhibit any peak. This suggests the possibility of achieving an optimum damping for some specific value of $1/\omega_o\tau$.

Fig. 4 shows, more quantitatively, the response amplitude at intermediate porosities. The curve for $1/\omega_o\tau = 3$ exhibits near-ideal behavior in the sense that one would not expect ringing to occur following a discontinuous change in the driving force. The response to a square-wave drive will be discussed in Section 9. Note too the node in the curves which according to Section 3.7 occurs at $\omega/\omega_o \approx \sqrt{1+\omega_g^2/2\omega_o^2} = \sqrt{3}$, where $A/F_0/m\omega_o^2) = 2\omega_o^2/\omega_g^2 = 1/2$.

Fig. 5 shows the magnitude B and the phase ϕ_2 of the pressure oscillations as a function of drive frequency. Curves are shown for several values of $1/\omega_o\tau$ and again with ω_g/ω_o fixed at 2.0. For comparison, Fig. 5c shows curves for ϕ_1, the phase of the displacement.

At $\omega = \omega_o$, the pressure oscillations have a magnitude which is independent of τ and are exactly in phase with the drive. At $\omega = \sqrt{\omega_o^2 + \omega_g^2}$, the magnitude of the pressure variations grows as the piston's porosity decreases. Here the pressure lags the drive by 90°, independent of the value of τ.

The phase of the piston's *displacement*, shown in Fig. 5c, exhibits a more complicated dependence on τ, with no

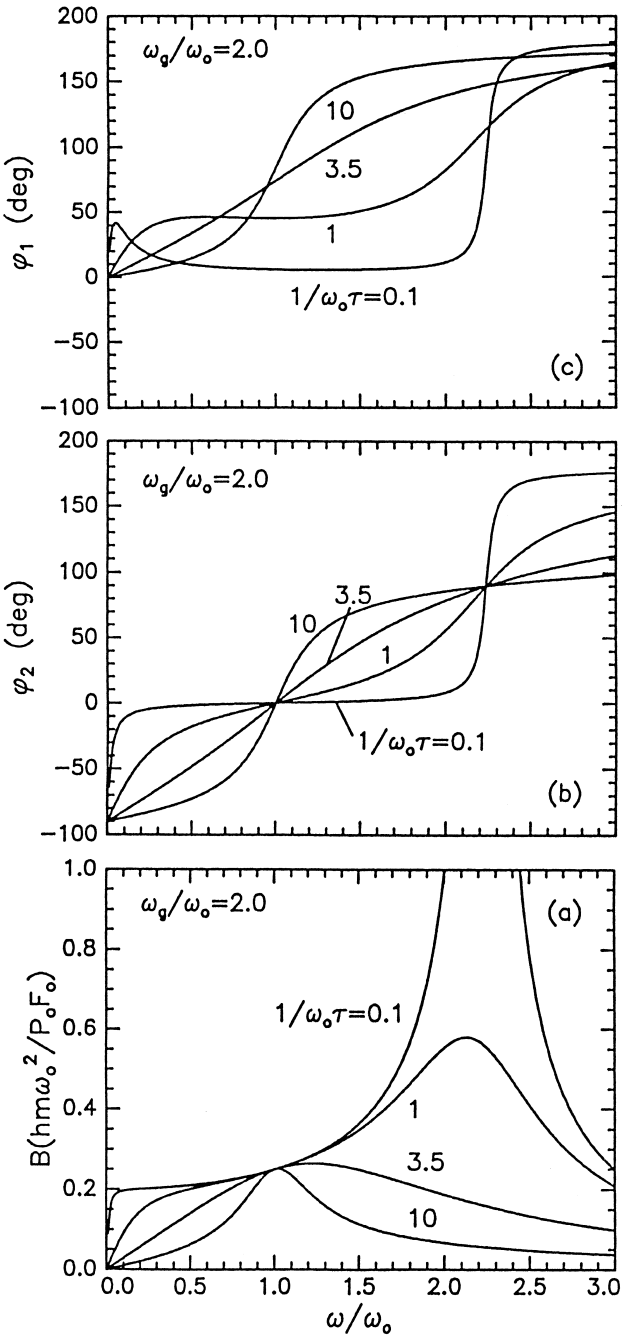

Fig. 5. Pressure amplitude (a) and phase (b) as functions of drive frequency. For comparison, (c) shows the phase of the displacement.

nodes. From this point of view, the pressure is the more fundamental parameter.

6. Constraint on ω_g for optimum damping

Fig. 4 of Section 5 suggests that a response curve showing no resonance peak can be achieved by adjusting only the piston's porosity. It is demonstrated here that this is not generally true and that ω_g/ω_o must be, in addition, sufficiently large.

The displacement amplitude A is plotted for several different fixed values of ω_g/ω_o in Fig. 6a,b,c. Fig. 6c has $\omega_g/\omega_o = 2$, as in Figs. 3 and 4. Fig. 6a,b show the corresponding curves with ω_g/ω_o fixed at 0.5 and 1.0, respectively. Note the different ordinate axis scales and the fact that the two curves with $1/\omega_o\tau = 1$ now have signifi-

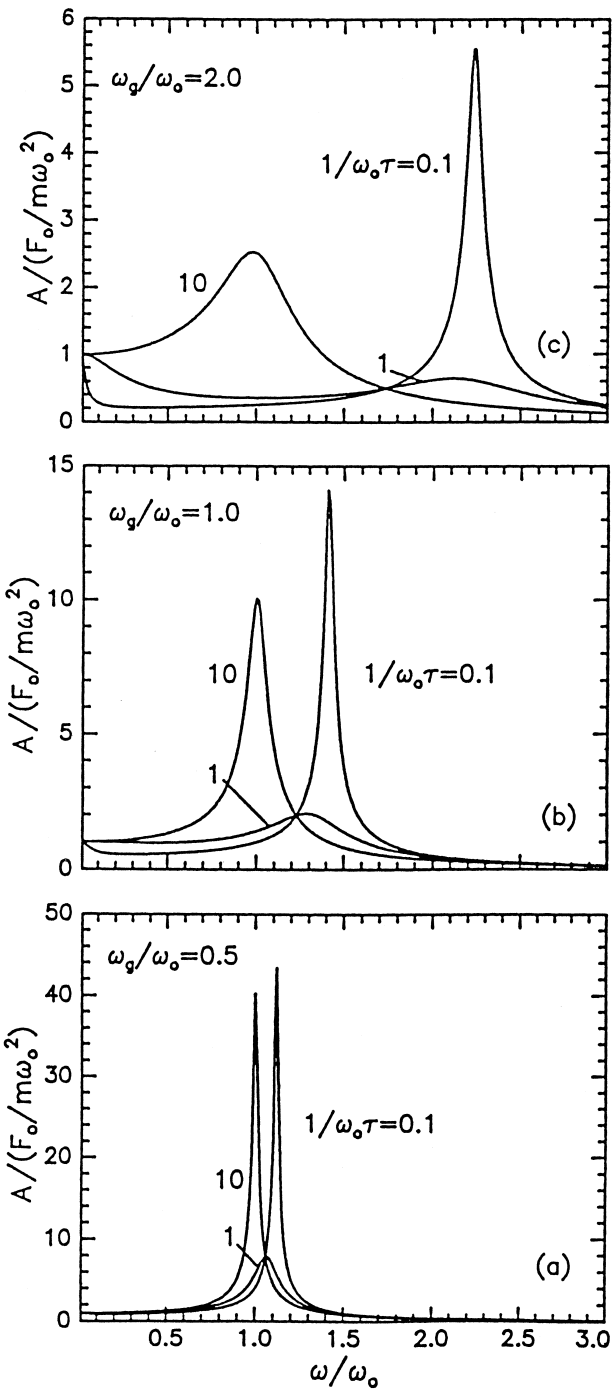

Fig. 6. Displacement amplitude vs. drive frequency. The curves in a, b, and c were computed with ω_g/ω_o fixed at 0.5, 1.0, and 2.0, respectively, and for several values of $1/\omega_o\tau$. Note that ω_g/ω_o plays an important role in determining the damping.

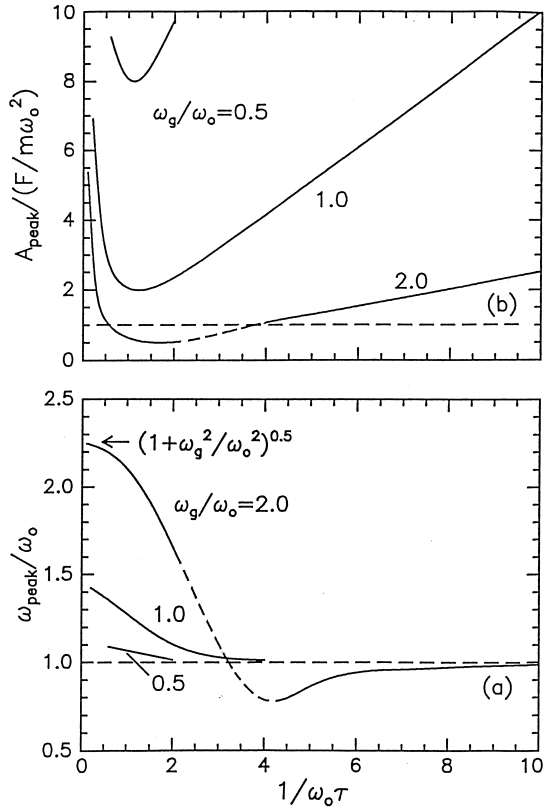

Fig. 7. Frequency (a) and displacement (b) at the resonance peak as a function of piston porosity. The dashed portions of the curves indicate the absence of a well-defined peak. The peak amplitude remains above unity for all values of $1/\omega_o\tau$, unless ω_g/ω_o is greater than about 2.

cant peaks, implying that it may be impossible to obtain sufficient damping at these smaller gas frequencies.

This is in fact the case as demonstrated in Fig. 7. Here the amplitude and frequency at the resonance peak are plotted as functions of the piston porosity. Curves are shown for ω_g/ω_o fixed at 0.5, 1.0, and 2.0. The dashed portions of the curves for $\omega_g/\omega_o = 2$ indicate the porosity region where the response curves do not exhibit a well-defined maximum. When $\omega_g/\omega_o = 0.5$, the reduced peak amplitude never drops below 8 (i.e., $Q \approx 8$); at $\omega_g/\omega_o = 1$ the minimum amplitude is 2. It is only at even higher reduced gas frequencies that the amplitude can be brought below unity and into a region of appreciable damping. Independent of the piston porosity, optimum damping cannot be achieved unless $\omega_g/\omega_o \geq 2$. This result is especially important for devices designed to work at frequencies above a few MHz, since it implies that the ambient gas pressure will have to be greater than atmospheric pressure.

7. Qualitative behavior of τ

At atmospheric pressure, the mean free path (mfp) of a gas molecule is of the order of a few tenths of a micron and so small compared to the dimensions of ordinary-sized systems, but comparable to the dimensions of typical micromechanical structures. The flow of gas within these devices, therefore, cannot be described as being either viscous or molecular. This makes quantitative theoretical calculations extremely difficult and dependent upon the particular device being modeled. Qualitatively, however, one would expect that at very low gas pressures (i.e., long mfp), τ would be a function of the molecule mass M and at high pressures, a function of the gas viscosity (Table 1).

Table 1
Gas parameters

Gas	Molecular weight, M	Viscosity (10^{-5} P)
H_2	2.02	9.0
He	4.00	20.0
Ne	20.18	32.1
Ar	39.94	22.9
Kr	83.80	25.6
Xe	131.30	23.2

Empirically, it is found (Section 11.4) that an expression of the form

$$\frac{1}{\tau} = \sqrt{\alpha^2 + \beta^2 P^2} \tag{25}$$

with

$$\alpha \sim M^{-1/4} \tag{26}$$

and

$$\beta \sim \eta^{-1/2} \tag{27}$$

can be used to accurately fit the experimental results for $0.5 < 3$ bars.

For the experimental devices to be discussed later, both the damping hole diameter and the center-to-center hole spacing are large compared to the gap spacing h (Fig. 8). Consequently, the gas is confined to flow parallel to the substrate and radially toward an opening with area $2\pi rh$. The rate at which gas escapes from under the piston is then determined not only by the size and number of these holes, but also by the impedance provided by the narrow gap.

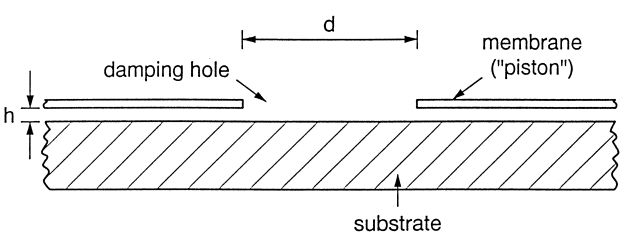

Fig. 8. Cross-section of a device in the region of a damping hole. The drawing is based on a hole diameter of 5 μm and a gap spacing of 0.4 μm.

8. Method for extracting ω_g and τ from frequency response curves

The mechanical frequency response of a device is mapped out experimentally by simply sweeping the frequency of a constant-amplitude driving force while detecting the amplitude of the resulting physical motion (see Section 11 for several examples). The exact shape of this curve will depend on the temperature, the pressure, and on the type of gas surrounding the structure. Of course, at zero pressure, there will be no gas damping and so, in general, one would expect a sharp resonance at the natural frequency f_o. As the pressure is increased from zero, the resonance peak decreases in amplitude and shifts in frequency. It is convenient to characterize each curve by two dimensionless quantities: f_{peak}/f_o and $A_{peak}/A_{\omega=0}$, where $A_{\omega=0}$ is the amplitude in the limit of zero frequency. Discussed in this section is the correspondence between these directly measured quantities and the two parameters of the model, namely ω_g/ω_o and $1/\omega_o\tau$.

Fig. 9a,b show ω_g/ω_o and $1/\omega_o\tau$ plotted vs. $A_{peak}/A_{\omega=0}$ along several curves corresponding to fixed values of ω_{peak}/ω_o. These curves were generated by numerically scanning ω_g/ω_o and $1/\omega_o\tau$ to search for pairs of values which imply, via Eq. (10), a resonance peak at a given fixed value of ω_{peak}/ω_o. The corresponding reduced amplitude $A_{peak}/A_{\omega=0}$ was also recorded. The curves in this figure were terminated at an abscissa value of unity to simplify the plot and also because at very small amplitudes, the resonance is broad and so, the uncertainty in f_{peak} is large. The termination at the opposite end of each curve is a consequence of the grid size used to scan values of ω_g/ω_o and the fact that all of the curves approach horizontal behavior at large amplitudes. Because each curve is single-valued as a function of amplitude, ω_g/ω_o and $1/\omega_o\tau$ can be determined uniquely given f_{peak}/f_o and $A_{peak}/A_{\omega=0}$.

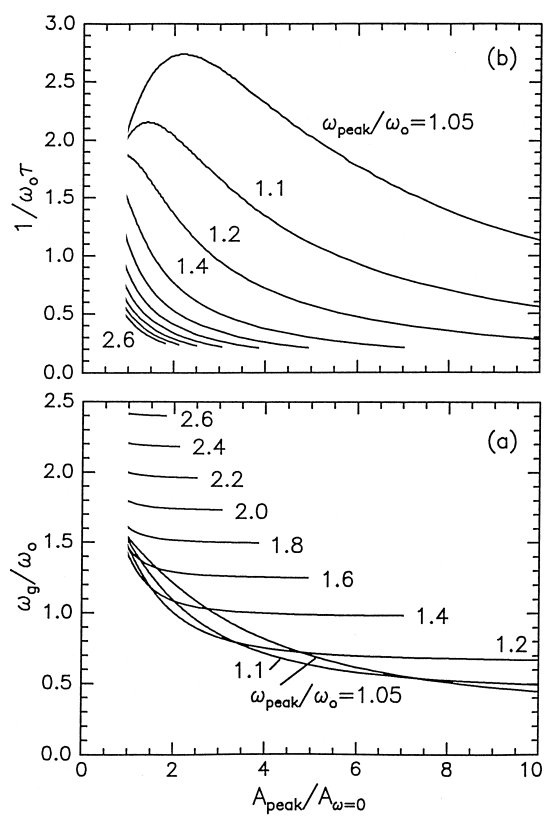

Fig. 9. Parameters ω_g/ω_o and $1/\omega_o\tau$ plotted vs. $A_{peak}/A_{\omega=0}$. These figures can be used to estimate the model parameters starting from a measurement of the frequency response curve.

As an example use of this figure, consider a device with a natural frequency of 1 MHz which under a given pressure has a resonance at 1.2 MHz with a reduced amplitude of 2. Following the curves with $\omega_{peak}/\omega_o = 1.2$ one finds that at $A_{peak}/A_{\omega=0} = 2$, ω_g/ω_o is about 1.0 and $1/\omega_o\tau$ is about 1.3. A simple modification of the computer program used to create Fig. 9 directly converted the experimental input values into the parameters of the model. For the above example, the routine yielded the more-quantitative values, $\omega_g/\omega_o = 1.003$ and $1/\omega_o\tau = 1.336$.

9. Response to a square-wave drive

High-speed switching applications require devices whose response to a discontinuous step change in drive exhibits a short rise time and no significant ringing. In this section, we determine the response to a square-wave drive by simply summing the complex frequency responses to the Fourier components of the drive signal.

A square-wave drive signal which switches between 0 and 1 with a period P can be written as the Fourier series

$$F(t) = \frac{1}{2} + \sum_{j=1,3,\ldots} \frac{2}{j\pi} \sin\left(\frac{2\pi jt}{P}\right). \tag{28}$$

It is convenient to use dimensionless quantities, and work with time measured in units of the natural period of the structure, i.e., $p_o = 1/f_o$.

With the definitions

$$\bar{t} = t/p_0, \tag{29}$$

$$P = P/p_0, \tag{30}$$

$$\bar{\omega}_j = \frac{\omega_j}{\omega_o} = \frac{2\pi j}{\bar{P}} \tag{31}$$

and

$$a_j = \frac{2}{j\pi}, \tag{32}$$

Eq. (46) can be written as

$$F(\bar{t}) = \frac{1}{2} + \Sigma a_j \sin\left(\bar{\omega}_j \bar{t}\right). \tag{33}$$

Summing the piston's complex frequency response corresponding to each of the Fourier components of the square-wave drive, the normalized response is

$$R(\bar{t}) = \frac{1}{2} + \sum_{j=1,3,\ldots} a_j \cdot \bar{A}(\bar{\omega}_j) \cdot \sin\left(\bar{\omega}_j \bar{t} - \phi_1\right). \quad (34)$$

The quantities $\bar{A}$ and ϕ_1 are given by Eqs. (22) and (23), which in reduced units take the forms

$$\bar{A} = Am\omega_o^2/F_o = \left\{\left[1 + \frac{\bar{\omega}_g^2}{1 + (\overline{\omega\tau})^{-2}} - \bar{\omega}^{-2}\right]^2 + \left[\frac{\bar{\omega}_g^2}{\overline{\omega\tau}} \cdot \frac{1}{1 + (\overline{\omega\tau})^{-2}}\right]^2\right\}^{-1/2} \quad (35)$$

and

$$\tan\phi_1 = \frac{\bar{\omega}_g^2/\overline{\omega\tau}}{(1-\bar{\omega})^2\left(1 + (\overline{\omega\tau})^{-2}\right) + \bar{\omega}_g^2}. \quad (36)$$

Here

$$\bar{\omega} = \omega/\omega_o, \quad (37)$$

$$\bar{\omega}_g = \omega_g/\omega_o, \quad (38)$$

and

$$\bar{\tau} = \omega_o\tau. \quad (39)$$

Fig. 10 shows several examples of square-wave response curves calculated using Eq. (34) (with $j_{max} = 301$) along with the corresponding frequency response curves based on Eq. (35). All of the curves are for $\omega_g/\omega_o = 2$; the different input values of $1/\omega_o\tau$ are indicated in the individual component plots.

For small values of $1/\omega_o\tau$, where the frequency response curves show a dramatic drop in amplitude at low frequencies, the square-wave response curves exhibit behavior which is characterized by two very-different time scales: the first is determined by τ, the second by $f_{peak} \approx \sqrt{f_o^2 + f_g^2} \approx \sqrt{5}$. For large values of $1/\omega_o\tau$, corresponding to a very porous piston, both of the response curves are very similar to those of an ordinary underdamped oscillator. Because f_{peak}, in this limit, is close to the natural frequency f_o, the ringing is now at a much lower frequency than in the low porosity regime.

Near-optimal response is achieved when $1/\omega_o\tau \approx 3$. Here the square-wave response has a rise time characterized by f_o and does not exhibit ringing, while the frequency response curve shows no remnant of any resonance peak.

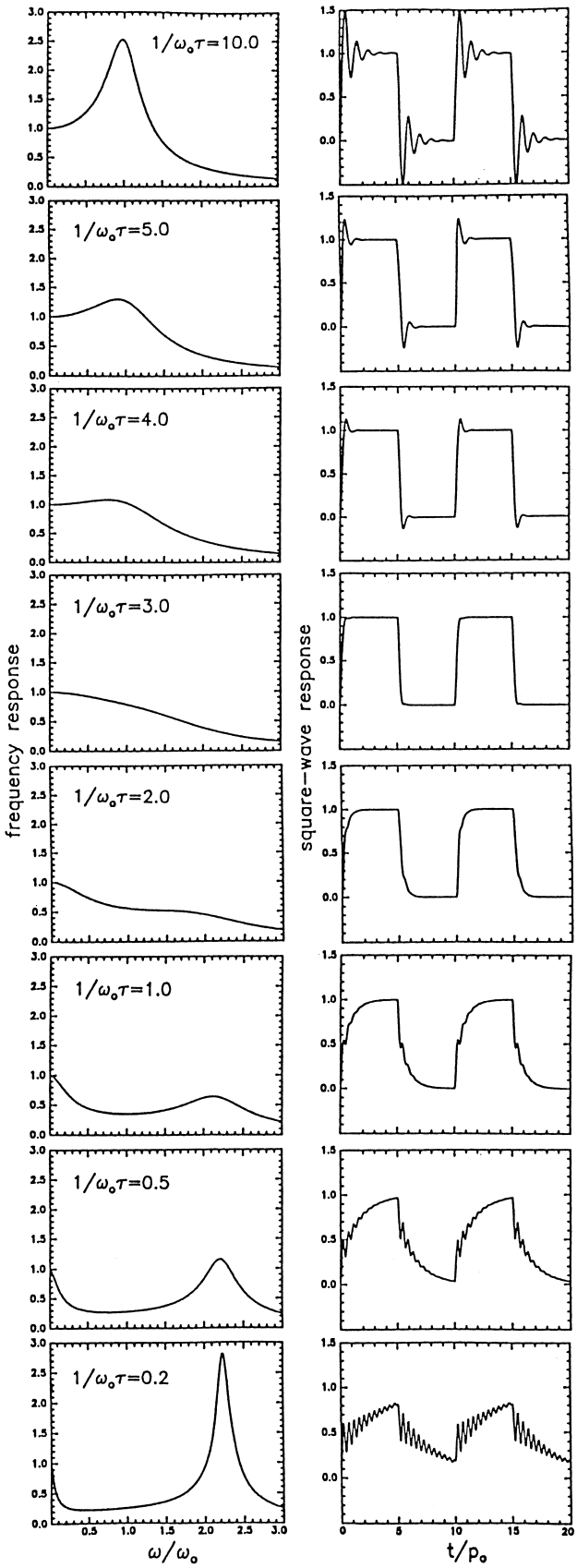

Fig. 10. Square-wave response corresponding to various frequency response curves. The calculations are for $\omega_g/\omega_o = 2$ and the values of $1/\omega_o\tau$ indicated. Time for the square-wave response curves is measured in units of the natural period $p_o = 1/f_o$.

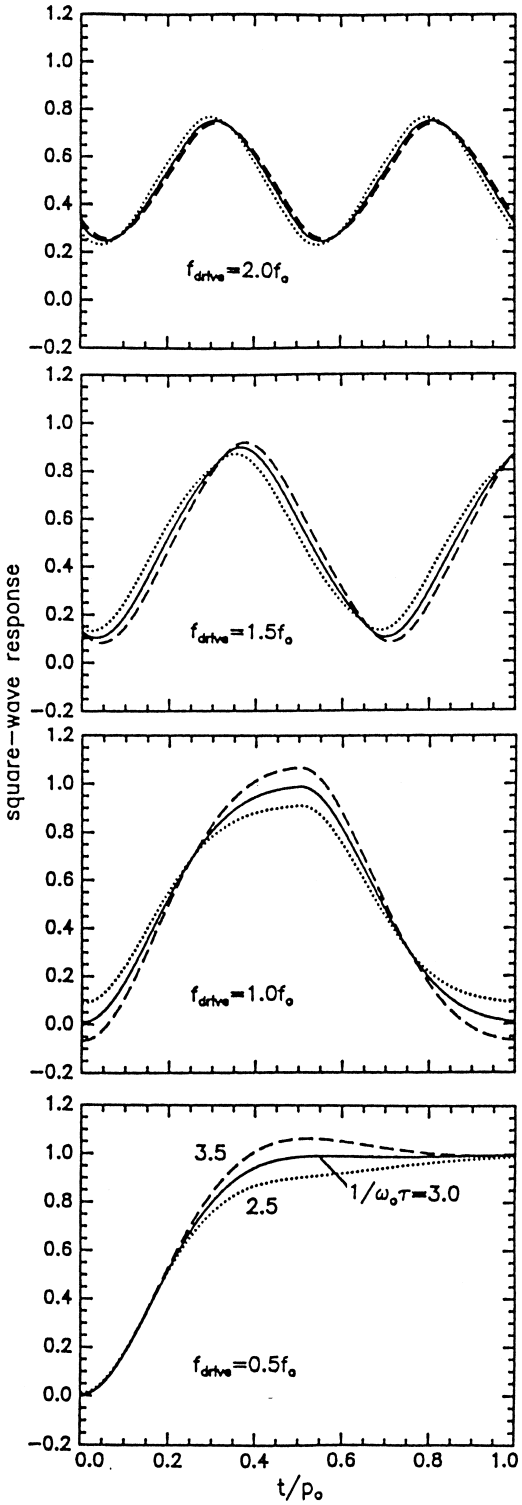

Fig. 11. Square-wave response for drive frequencies of the order of f_o. The curves were computed using $\omega_g/\omega_o = 2$ and the values of $1/\omega_o\tau$ indicated.

Fig. 11 shows the square-wave response of this optimal device when the drive frequency is greater than f_o. Curves are also included for $1/\omega_o\tau = 2.5$ (dotted) and for $1/\omega_o\tau = 3.5$ (dashed). As the drive frequency is increased above f_o, the full amplitude swing between 0 and 1 can no longer be achieved. However if, for example, a swing between 0.1 and 0.9 is acceptable, then, the operating range can be extended to $1.5f_o$, which implies a bit rate of about $3f_o$.

10. ω_g/ω_o and $1/\omega_o\tau$ for optimum square-wave response

In Section 9, it was demonstrated that nearly ideal small-amplitude, square-wave response could be achieved for one particular pair of parameters, namely $\omega_g/\omega_o = 2$ and $1/\omega_o\tau = 3$. Other pairs of values, however, will yield similar results. In this section, a more general relationship for optimum response is mapped out.

The range of parameter values giving acceptable square-wave response was extracted from plots similar to the one shown in Fig. 12. Here the response calculated using Eq. (34) is plotted vs. time measured in units of the natural period. For this example, the parameter ω_g/ω_o is fixed at 2.0 and the individual curves correspond to various values of $1/\omega_o\tau$ ranging from 1 to 5.

The amount of ringing was quantified simply by considering the normalized amplitude of response at a time $p_o/2$ following an instantaneous step in the drive signal. The dashed horizontal lines in the figure correspond to the upper and lower amplitudes for '10% ringing'. The larger amplitude is reached when $1/\omega_o\tau = 3.8$; the lower when $1/\omega_o\tau = 2.4$. So if $\omega_g/\omega_o = 2$ and $2.4 \le 1/\omega_o\tau \le 3.8$, the square-wave response will show less than 10% ringing. If $2.7 \le 1/\omega_o\tau \le 3.4$, the ringing will be less than 5%.

The limits on $1/\omega_o\tau$ determined for various values of ω_g/ω_o were used to map out the 5% and 10% boundaries in a plot of $1/\omega_o\tau$ vs. ω_g/ω_o (Fig. 13). There are sizable ranges of acceptable values for both parameters; also there are threshold values for both parameters: ω_g/ω_o must be greater than about 1.5 and $1/\omega_o\tau$ must be greater than

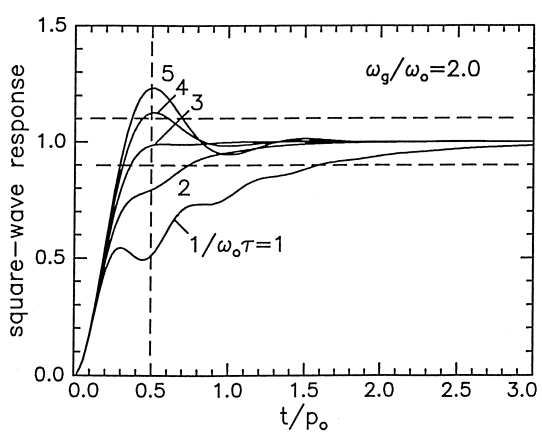

Fig. 12. Response to a discontinuous change in the drive for times comparable to the natural period p_o. The dashed lines define '10% ringing'. Fig. 10 shows these curves extended to longer times.

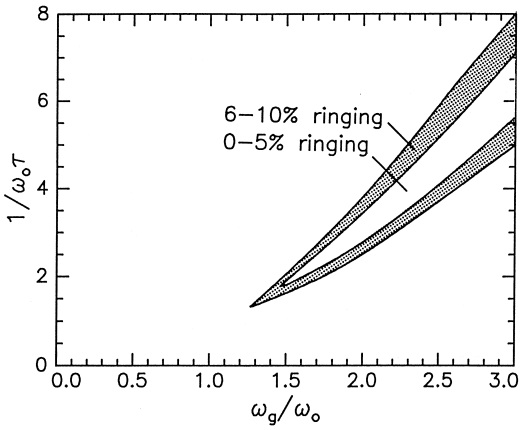

Fig. 13. Relationship between ω_g/ω_o and $1/\omega_o\tau$ which must be satisfied in order to achieve near-optimum square-wave response.

about 2.0. If ω_g/ω_o is not greater than 1.5, a clean square-wave response cannot be achieved, independent of the piston's porosity.

11. Comparison with experiment

Detailed measurements were made on eight micromachined devices. Each had the structure of a cylindrical drum with a stressed (800 MPa) drumhead membrane of silicon nitride. The membrane was covered with an annular metal plating (100 Å of Ti, 500 Å of Au). This electrode and the doped silicon substrate formed a capacitor, allowing the resonator to be excited electrostatically. The resulting motion of the membrane was detected by measuring the modulation in the reflectivity of the unplated, transparent central portion of the membrane. Interference effects alter the reflectivity because the thickness (0.195 μm) of the membrane as well as the size of the gap under the membrane are both comparable to the optical wavelength.

Fig. 14 shows schematically, but to scale, the four damping hole arrangements examined. Each of these layouts was used with two different gap spacings, namely: 0.39 μm and 0.97 μm, accounting for the eight test devices. The dashed circle indicates the size of the drumhead; the dark shading shows the metal electrode; and the small white circles indicate the damping holes which pass through both the electrode and the membrane. These holes have diameters of either 3 or 5 μm and lie on circles with diameters of 40, 70, or 100 μm. The drumhead diameters are 150 μm for (a), (b), and (c) and 120 μm for (d). Various parameters for each of the test devices are listed in Table 2, along with the assigned sample numbers used throughout this section.

11.1. Frequency response: peak amplitude and frequency

Examples of measured small-amplitude ($A/h \preceq 10^{-3}$) frequency response curves are shown in Figs. 15 and 16,

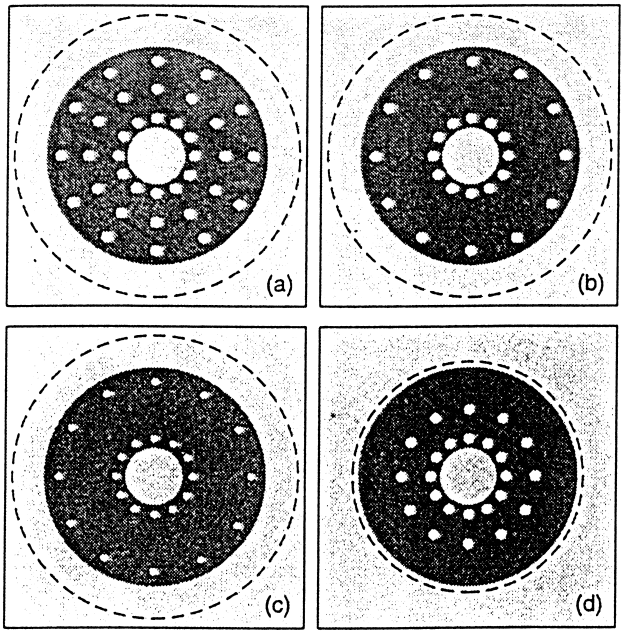

Fig. 14. Top-view schematics of the drumhead structures studied experimentally. Each layout was used with two different gap spacings accounting for a total of eight test devices. The dashed circle indicates the size of the drumhead; the dark shaded region shows the region covered by a metal electrode; and the small white circles indicate the size and location of the damping holes which pass through the electrode and membrane.

with the various curves in each plot corresponding to different helium pressures ranging from 0.2 to 3 bars. Each of the curves has been normalized so that at zero frequency, the amplitude is unity. The small peak near 5 MHz in Fig. 15 is a higher-order mode not included in our simple model.

The measured response is obviously very different for these two samples: Sample 5 exhibits a rather standard set of resonance curves with the low frequency amplitude rising monotonically from unity. The peak frequency shifts by only 10% over the entire pressure range. In contrast to this behavior, Sample 2 shows a low frequency amplitude which drops well below unity at the higher pressures. And now, the peak frequency more than doubles with increasing pressure. Note that both of the samples have the hole

Table 2
Parameters for the drumhead text devices

Sample number	D (μm)	h (μm)	N	d (μm)	f_o (MHz)	$f_g/\sqrt{P}$ (MHz/bar$^{1/2}$)
1	150	0.39	36	5	2.14	2.6
2	150	0.39	24	5	2.02	2.6
3	150	0.39	24	3	2.06	2.6
4	150	0.97	36	5	2.19	1.5
5	150	0.97	24	5	2.15	1.3
6	150	0.97	24	3	2.26	1.4
7	120	0.39	24	5	2.94	2.6
8	120	0.97	24	5	2.67	1.3

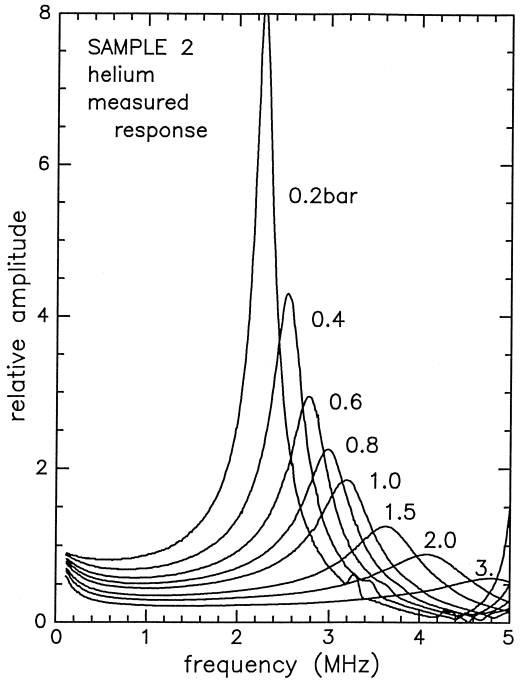

Fig. 15. Measured resonance curves for Sample 2 at various helium pressures. This sample has the damping hole arrangement shown in Fig. 14b and a gap spacing under the membrane of 0.4 μm.

arrangement shown in Fig. 17b and the same natural frequency, 2 MHz. They differ only in gap size.

The frequency and amplitude of the measured resonance peaks, extracted from plots similar to Figs. 15 and 16, are plotted vs. pressure in Figs. 17 and 18. These data are for devices 1–6, all of which have the same diameter (150 μm) and the same natural frequency f_o (2 MHz). Samples 1–3 have the small gap spacing, Samples 4–6 have the larger gap. Note the different ordinate scales for each row of figures. The sample pairs 1 and 4, 2 and 5, and 3 and 6 have the same damping hole arrangements corresponding to Fig. 16a,b,c. Frequency and amplitude data for Samples 7 and 8, with the smaller drumhead diameter are shown in Fig. 19, and only for helium.

Using these complicated results as input, corresponding values of ω_g/ω_o and $1/\omega_o\tau$ were extracted according to the discussion in Section 8. As demonstrated later, these derived quantities behave more simply and permit an understanding of the experimental observations.

11.2. Anomalous results for Ar and Xe

Compared to data obtained for the lighter gases, the frequency response curves for Ar and Xe often showed more complicated resonance behavior, making it difficult, and sometimes impossible, to extract meaningful information. An attempt is made here to explain these observations.

Fig. 20 shows response curves for Sample 5 obtained using various gases, all at a pressure of 3 bars. The curves for H_2, He, and Ne are smooth and show no unusual features. In contrast to this, the results for Ar show some structure near 4 MHz, while the Xe curve actually exhibits a well-defined anomalous peak near 2 MHz. The frequency of this peak does not shift with drive amplitude or with pressure. Sample 2, which is identical to Sample 5 except for the smaller gap size, does not show a peak at 2 MHz, but instead a large interference signal near 3.6 MHz.

The fact that f_{anom} is independent of pressure immediately suggests a sound resonance in the gas within the device. The fundamental plane-wave mode has a resonance frequency given by

$$f_{pw} = v_{gas}/2t_{gap} \tag{40}$$

with

$$v_{gas} = \sqrt{\gamma RT/M} \tag{41}$$

for an ideal gas. Using $v_{Xe} \approx 180$ m/s and $t_{gap} \approx 1$ μm implies $f_{pw} \approx 90$ MHz, which is more than an order of a magnitude too large.

Purely transverse vibrations, however, can have much lower frequencies. These resonances are determined by the relation [14]

$$f_{mn} = \frac{v_{gas}\alpha_{mn}}{D}, \tag{42}$$

where D is the diameter of the cylindrical chamber, α_{mn} is a solution of $d[J_m(\pi\alpha)]d\alpha = 0$, and $J_m(\pi\alpha)$ is a Bessel function of the first kind. Using $D = 150$ μm and the sound velocity for Xe, Eq. (42) predicts possible resonances (in MHz) at $f_{01} = 1.5$, $f_{02} = 2.7$, $f_{03} = 3.9$, $f_{11} =$

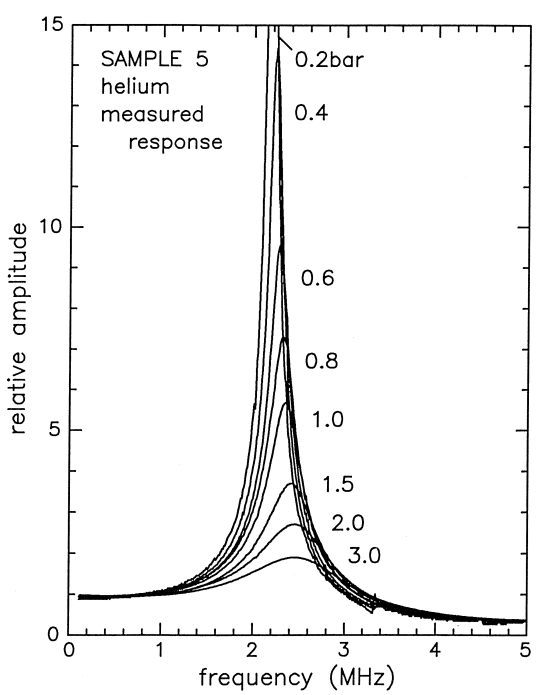

Fig. 16. Measured resonance curves for Sample 5 in helium. This sample is identical to Sample 2 (Fig. 15) except the gap spacing is now 1.0 μm.

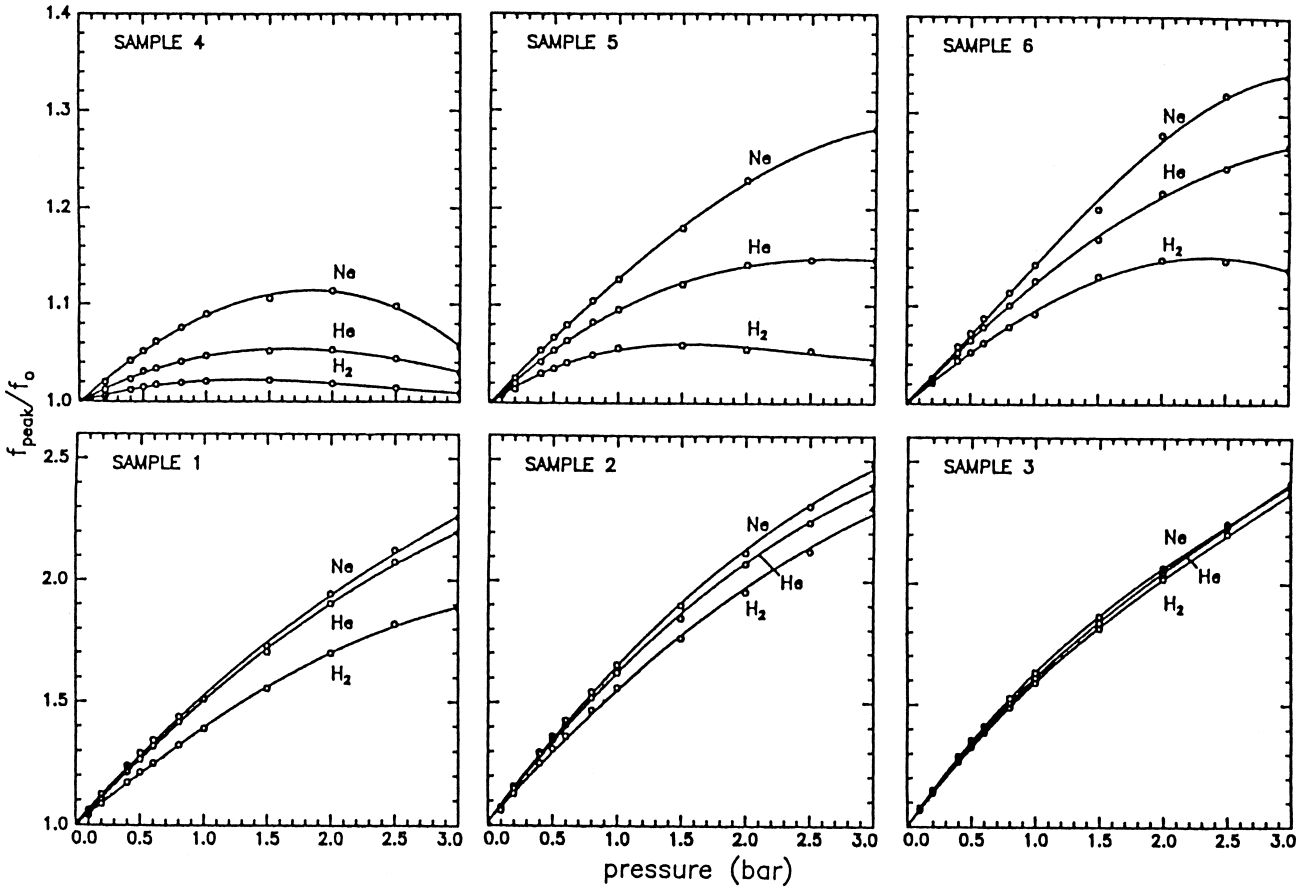

Fig. 17. Measured peak frequencies for Samples 1–6 in H_2, He, and Ne. Samples 1–3 have a gap of 0.4 μm; Samples 4–6 have a gap of 1.0 μm. Note the different vertical scales for each row of figures.

0.7, $f_{12} = 2.0$, and $f_{13} = 3.2$, which are of the proper magnitude. A direct comparison of numbers suggests that the anomaly near 2.2 MHz for Sample 5 may be the f_{12} mode, while the peak for Sample 2 at 3.6 MHz may be the f_{13} mode.

According to Eqs. (41) and (42), the transverse resonances in the gas are proportional to $M^{-1/2}$ and so, are pushed to much higher frequencies for the lighter gases, explaining the absence of anomalies in these data.

Because the anomaly for the large-gap samples occurred near f_o (presumably by accident), the low pressure Xe curves were ambiguous. On the other hand, the small gap samples, with the anomaly at a much higher frequency, could be analyzed if the pressure was not too high. Figures in the later sections will therefore only include Ar and Xe results for Samples 1–3.

11.3. Results for ω_g / ω_o

Fig. 21 shows ω_g/ω_o plotted vs. $P^{1/2}$ for Samples 2 and 5. It is immediately evident that (1) ω_g/ω_o is proportional to $P^{1/2}$, (2) ω_g/ω_o is independent of gas type, and (3) ω_g/ω_o generally varies inversely with the gap spacing. Each of these observations agrees with expectations based on Eqs. (7) and (24). This self-consistency, which will be examined in the remainder of this section, supports the application of the model to this particular set of devices.

Although Samples 1–3 differ in the damping hole arrangement, the dimensions of the cylindrical cavity under the membrane are the same and so, from Eq. (7), the gas frequencies should be identical. Indeed, it is found that $f_g/P^{1/2} = 2.6$ for each of these devices.

The corresponding parameters for the larger gap structures Samples 4–6, should also be the same. But here, a greater variation is found, with the value for Sample 4 being 15% larger than the values for Samples 5 and 6. The discrepancy is correlated with f_g also showing a weak dependence on gas type, for pressures below 1 bar. Note though, that the uncertainties in the extracted model parameters for the large-gap samples are larger because the measured frequency shifts are very small (Fig. 17). Weighing the results for Samples 5 and 6 more heavily, the conclusion is that the value for these devices is $f_g/P^{1/2} = 1.3$.

Fig. 22 shows ω_g/ω_o data for Samples 7 and 8 which were obtained using helium. These devices are smaller in

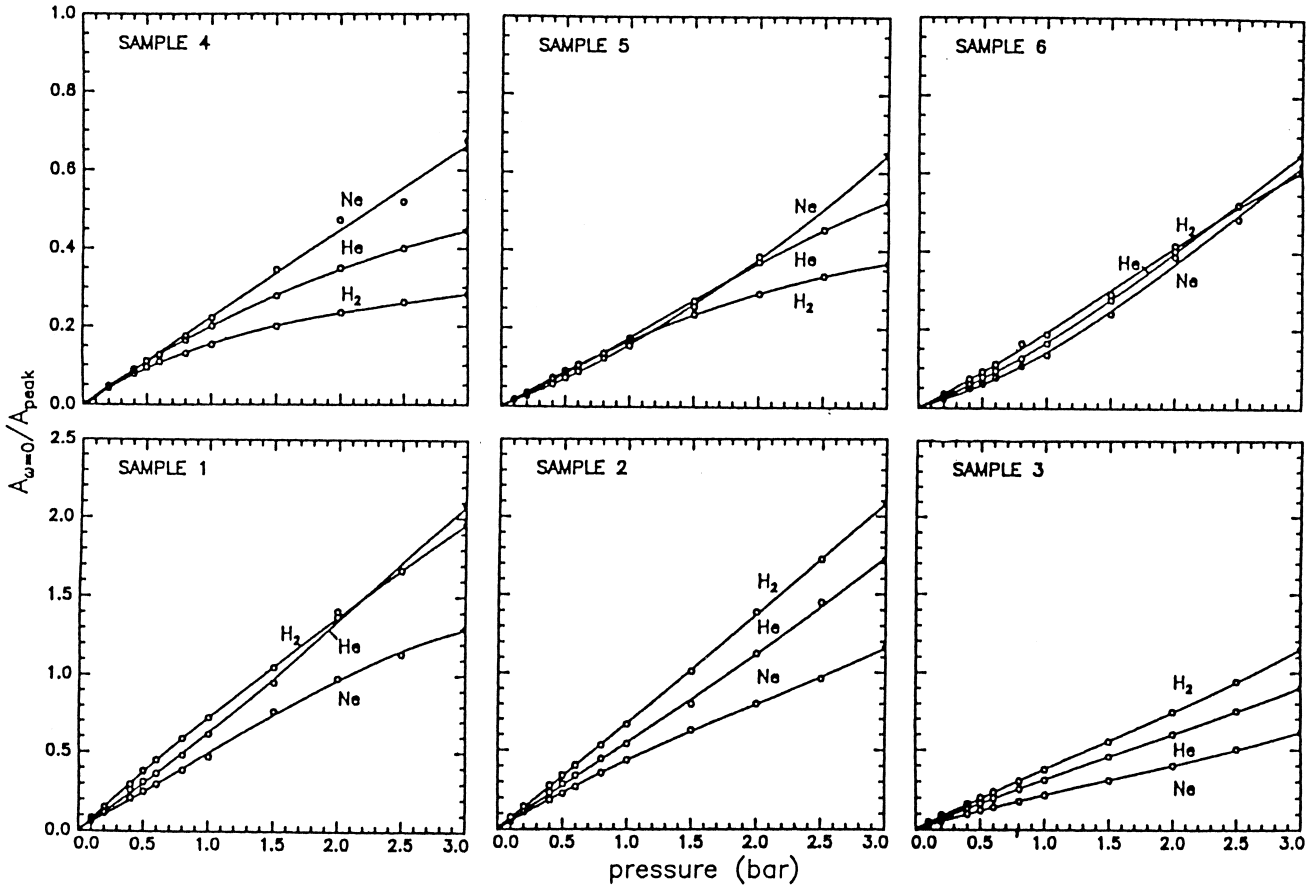

Fig. 18. Measured peak amplitudes for Samples 1–6. Note the different vertical scales for each row of figures.

diameter and have a much higher natural frequency. Again, the same values were extracted, namely $f_g/P^{1/2} = 2.7$ for the small gap sample and 1.3 for Sample 8, demonstrating explicitly that this quantity does not depend on device diameter.

A direct evaluation of Eq. (24) yields $f_g/P^{1/2} = 2.4$ MHz/bar$^{1/2}$ for the small gap samples ($h = 0.39$ μm, $t = 0.19$ μm, and $\bar{\rho} = 5.9\,\mathrm{gm/cm^3}$) and 1.4 MHz/bar$^{1/2}$ for the large gap devices ($h = 0.97$ μm, $t = 0.23$ μm, and $\bar{\rho} = 5.9\,\mathrm{gm/cm^3}$). Given the uncertainties in the input parameters, the 10% agreement with the measurements is acceptable.

11.4. Results for τ

In this section, the $1/\omega_o\tau$ data are analyzed and are described in terms of simple empirical relations. These expressions help to give the model predictive power.

Fig. 23 shows $1/\omega_o\tau$ for Samples 1–6; Fig. 24 shows data for Samples 7 and 8. These curves are qualitatively much simpler than the measured input data shown in Figs. 17 and 18. Consistency with the functional form of Eq. (25) is demonstrated in Fig. 25, where $(1/\omega_o\tau)^2$ is plotted vs. P^2. The intercepts and slopes of the three straight lines drawn in the figure determine $(\alpha/\omega_o)^2$ and $(\beta/\omega_o)^2$ for each of the corresponding gases.

The deviations from the straight lines at low pressures are systematic and are shown in greater detail in Fig. 26. These particular data are for Sample 1 in H_2 but are representative of the results for other samples and other gases. The dip in the curve is presumably the Knudsen minimum seen in ordinary gas flow measurements [15] and also in thermal conductivity data [16] when the mean free path of the particles or (phonons) is comparable to the dimensions of the tube. Because this behavior is confined to low gas pressures, it is ignored in the following analysis.

As already discussed in Section 7, both α and β are expected to be functions of the various physical dimensions of the device. In addition, α should depend on the molecular mass and β on the gas viscosity. Fitting the α and β values for each sample to various simple power-law expressions, it was determined that

$$\alpha = \alpha_o / M^{\frac{1}{4}} \tag{43}$$

and

$$\beta = \beta_o / \eta^{\frac{1}{2}} \tag{44}$$

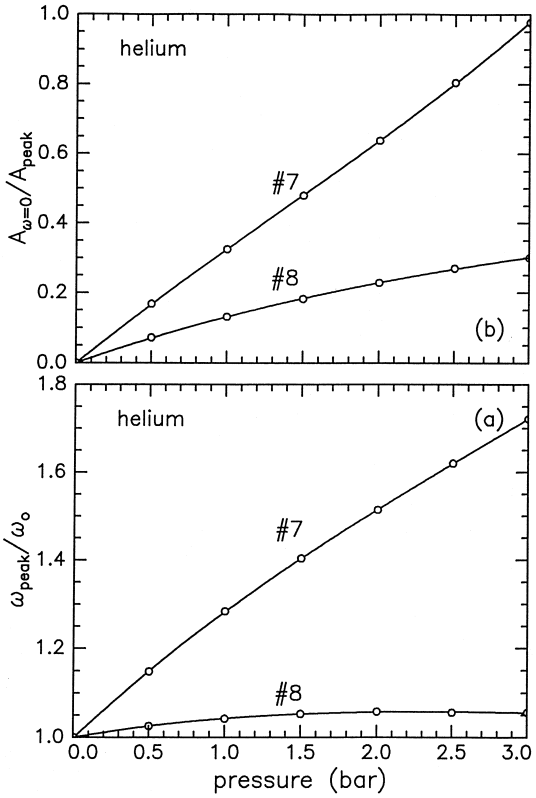

Fig. 19. Measured peak frequency and amplitude for Samples 7 and 8. These devices have a smaller drumhead diameter than Samples 1–6.

represented the data well. The parameters α_o and β_o are dependent on device geometry and so, are different for each sample.

To reduce the uncertainties in the best-fit parameters due to correlations, the $1/\omega_o\tau$ data were refit using the expression

$$\frac{1}{\omega_o\tau} = \left[\left(\frac{\alpha}{\omega_o}\right)^2 + \left(\frac{\beta_o}{\omega_o\eta^{1/2}}\right)^2 P^2\right]^{1/2} \quad (45)$$

yielding for each device a single value for β_o and values

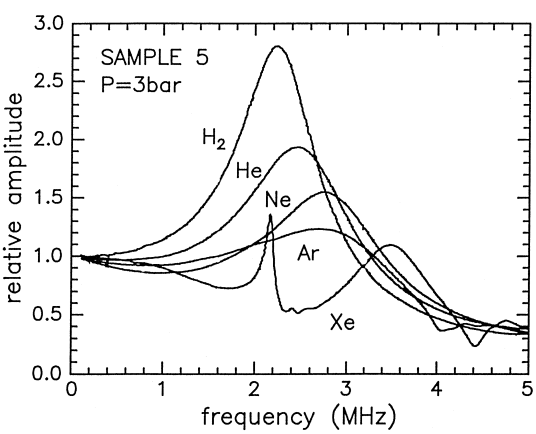

Fig. 20. Resonance curves for Sample 5 measured using various gases at 3-bar pressure. The anomalous peak in the xenon curve near 2 MHz is due to a radial sound mode in the gas.

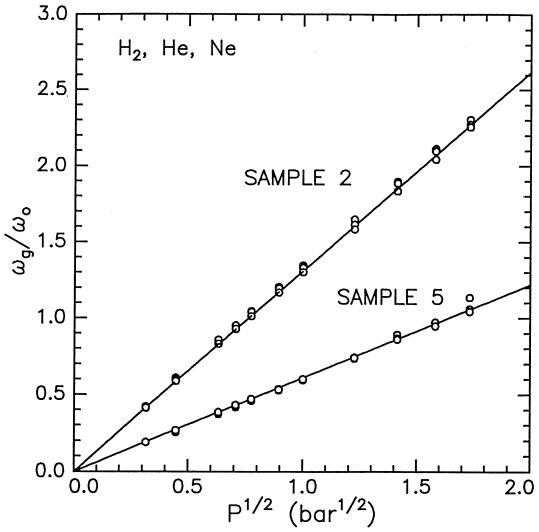

Fig. 21. ω_g/ω_o results for Samples 2 and 5. Note that this parameter is independent of gas type, proportional to $P^{1/2}$, and larger for the small-gap sample.

for α corresponding to each of the gases used. Fig. 27 shows these best-fit values of α plotted vs. $M^{-1/4}$ to demonstrate the simple proportionality between these two quantities. The only significant deviations from the straight lines in this figure occur for hydrogen and the large-gap samples. The difficulties with the hydrogen results are ignored, and emphasis is placed on the monatomic rare gas data. The slope of each straight line in Fig. 27 determines α_o/ω_o for each device.

Fig. 28a,b show α_o/ω_o and β_o/ω_o plotted vs. *Nd*. To a good approximation, these parameters are found to be simply proportional to the total circumference of all of the damping holes in the membrane. Moreover, the ratio of the slopes of the two lines in Fig. 28a is 2.4. For Fig. 28b, the ratio is again 2.4. This number is within the experimental

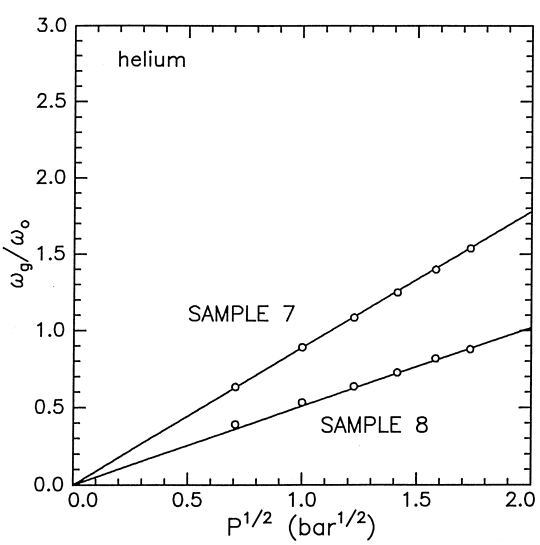

Fig. 22. ω_g/ω_o results for Samples 7 and 8 in helium.

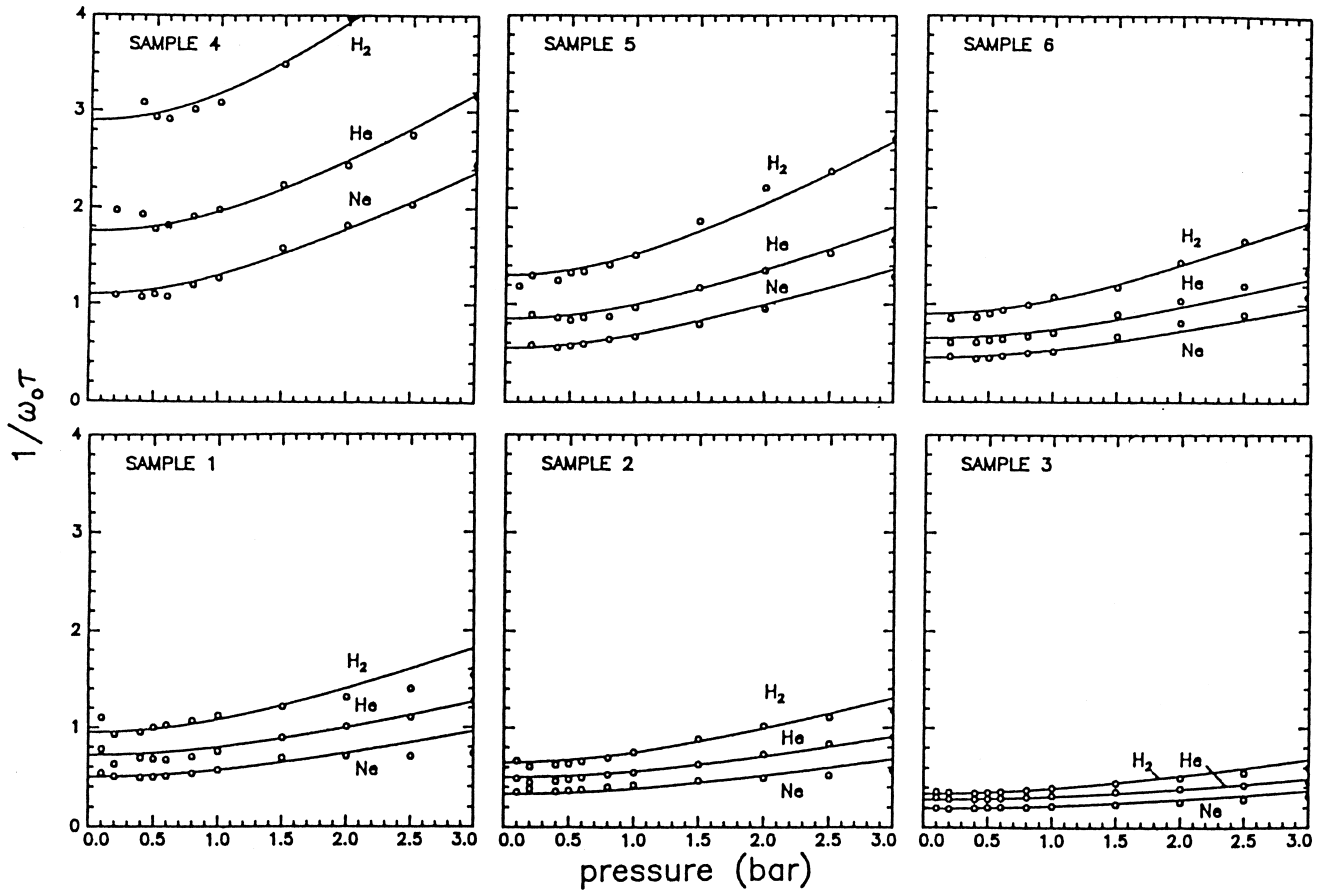

Fig. 23. $1/\omega_o\tau$ results for Samples 1–6. Note that this parameter has a much simpler pressure dependence than the measured data shown in Figs. 17 and 18.

uncertainties equal to the ratio of the gap spacings, namely: $0.97/0.39 = 2.5$.

Bringing these observations together and using an average value for ω_o, namely: $2\pi 2.15$ MHz, leads to

$$\alpha = 1.89 \times 10^5 \, Ndh/M^{\frac{1}{4}} \tag{46}$$

and

$$\beta = 2.77 \times 10^5 \, Ndh/\eta^{1/2}. \tag{47}$$

Thus, for Samples 1–6,

$$\frac{1}{\tau} = 1.89 \times 10^5 \frac{Ndh}{M^{\frac{1}{4}}} \left[1 + \frac{2.1 M^{1/2} P^2}{\eta} \right]^{1/2}. \tag{48}$$

The comparison of Eqs. (8) and (48) indicates that the effective porosity ξ goes as h^2.

According to Eq. (9), $1/\tau$ should be inversely proportional to the area of the device or to D^2. The explicit dependence on D^2 can be introduced into Eq. (48) by multiplying the right hand side by $(150 \ \mu m/D)^2$, which for Samples 1–6 is unity. This leads to the general relation

$$\frac{1}{\tau} = 4.3 \times 10^9 \frac{Ndh}{D^2 M^{\frac{1}{4}}} \left[1 + \frac{2.1 M^{1/2}}{\eta} P^2 \right]^{1/2}. \tag{49}$$

Again, N is the number of damping holes of diameter d,

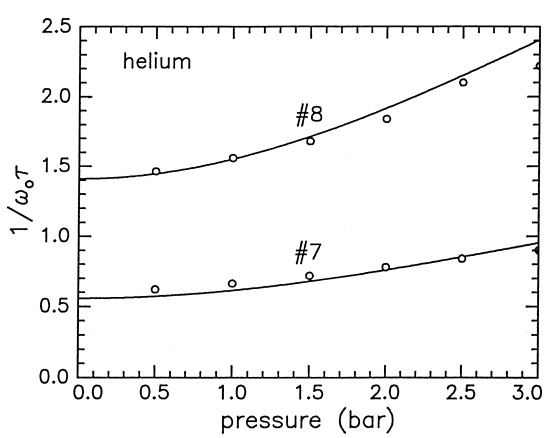

Fig. 24. $1/\omega_o\tau$ results for Samples 7 and 8.

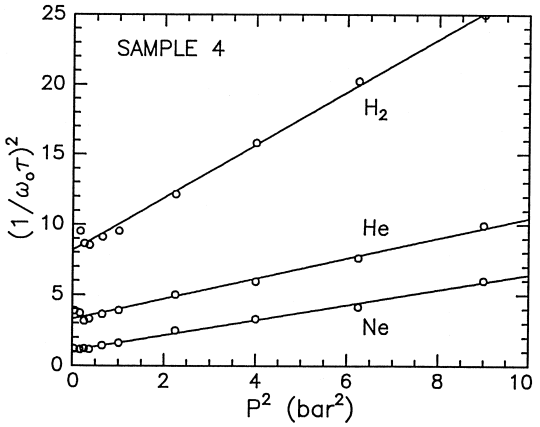

Fig. 25. $1/\omega_o\,\tau$ results for Sample 4 plotted to show consistency with the functional form $1/\omega_o\tau = (\alpha^2 + \beta^2 P^2)^{1/2}$. The parameters α and β have different values for each gas and for each device.

which are distributed 'uniformly' over the membrane, D is the device diameter, h is the gap spacing, η is the viscosity in units of 10^{-5} P, and P is the pressure in bar.

The $1/\omega_o\tau$ data for Samples 7 and 8 were not used in extracting Eq. (49) and so, could be used to check this expression. These devices have $D = 120$ μm, $d = 5$ μm, and $N = 24$. Sample 7 has $h = 0.39$ μm and $f_o = 2.94$ MHz; Sample 8 has $h = 0.97$ and $f_o = 2.67$ MHz. Substituting these numbers into Eq. (49) yields

$$\frac{1}{\omega_o\tau}\Big|_{\#7,\mathrm{He}} = 0.53\left(1 + 0.21P^2\right)^{1/2} \tag{50}$$

and

$$\frac{1}{\omega_o\tau}\Big|_{\#8,\mathrm{He}} = 1.45\left(1 + 0.21P^2\right)^{1/2}. \tag{51}$$

These equations describe the experimental data well and were used to plot the solid curves shown in Fig. 24.

A further test of the model was made by computing resonance curves using Eq. (10) with ω_g/ω_o given by Eq. (24) and $1/\omega_o\tau$ given by Eq. (49). Figs. 29 and 30 show curves based on the physical parameters describing Samples 2 and 5, respectively. These figures can be compared directly with the experimental curves in Figs. 16 and 17. The largest differences occur near zero frequency for Sample 2. This sample has a small gap and a small value of $1/\omega_o\tau$. The breakdown of the model in this regime is associated with the neglect of the Γ term in Eq. (10).

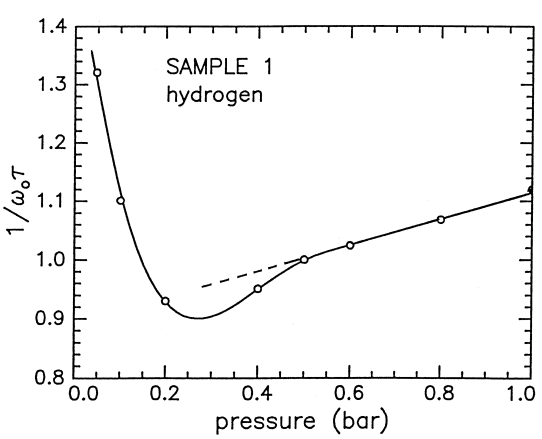

Fig. 26. $1/\omega_o\tau$ results at low pressures showing the Knudsen minimum.

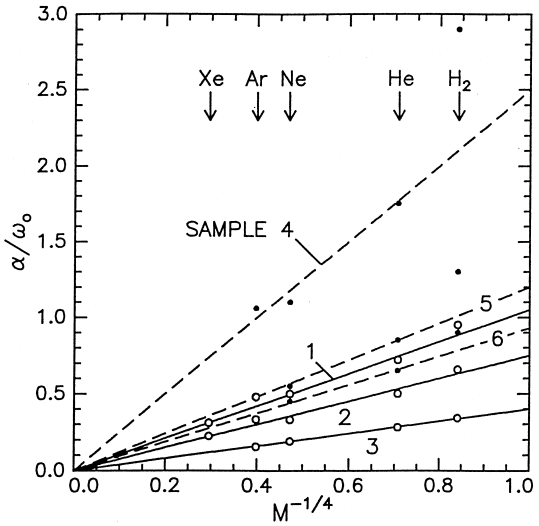

Fig. 27. Plot showing proportionality between α and $M^{-1/4}$ for Samples 1–6 and for the rare gases. The H_2 values for the large-gap samples depart from this simple relationship.

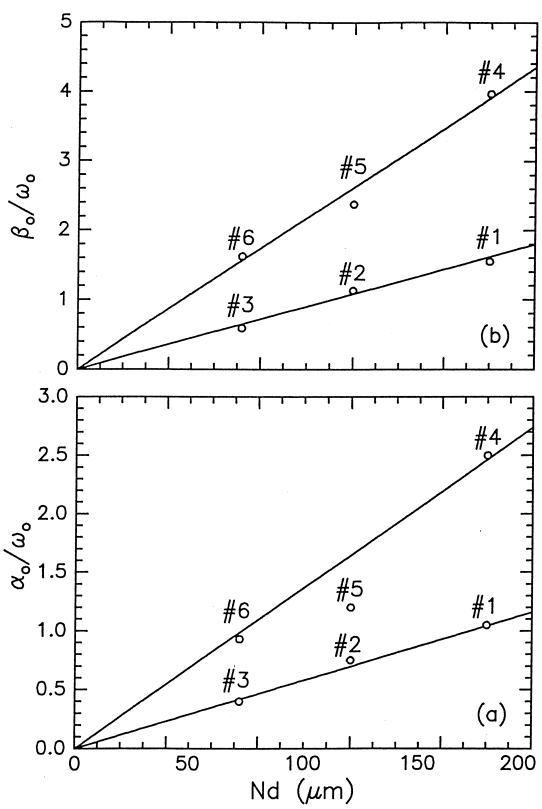

Fig. 28. Parameters α_o and β_o for Samples 1–6 as a function of the total circumference of all of the damping holes in the membrane. The simple results give the model predictive power.

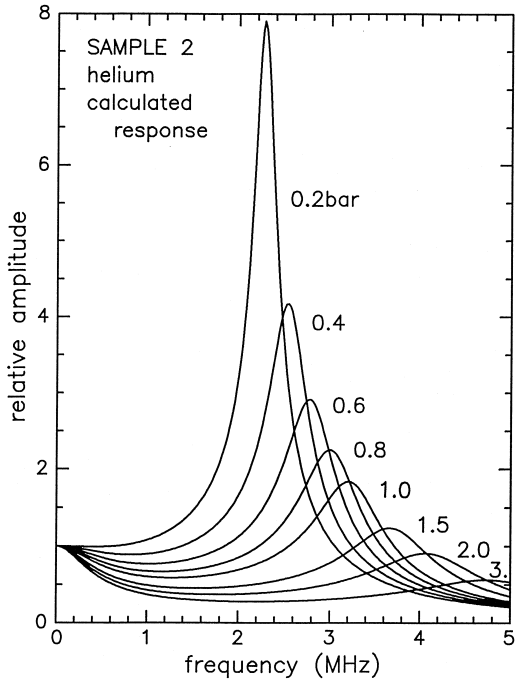

Fig. 29. Calculated resonance curves for Sample 2. There is excellent agreement with the data shown in Fig. 15, except at the lowest frequencies.

11.5. Square-wave response

Measured and calculated square-wave response curves are compared in Fig. 31, which shows results for Sample 1 in H_2, and in Fig. 32 which shows results for Sample 5 in He. The calculated curves are based on the empirical expressions for ω_g/ω_o and $1/\omega_o\tau$, i.e., Eqs. (24) and (49), and were computed according to the discussion in Section 9. The large noise amplitude in the experimental curves for Sample 5 is explained by the fact that the membrane thickness and the gap size were not properly paired to give a strong optical signal. Nonetheless, detailed agreement between measured and calculated response is apparent in both figures.

Although the ringing for Sample 1 is completely suppressed by a gas pressure above 2 bars, the price for this is a slow rise time. Ringing for Sample 5 (with the larger gap size) is more severe and persists to the highest test pressures. The two samples therefore deviate in behavior to opposite sides of optimum response.

11.6. Devices with optimum response

Fig. 13 of Section 10 shows the range of ω_g/ω_o and $1/\omega_o\tau$ values leading to optimum square-wave response. In this section, the test devices are located in this parameter space with mappings that show the paths followed as the ambient gas pressure is changed.

According to Eqs. (7) and (25),

$$\omega_g = \gamma P^{1/2} \tag{52}$$

and

$$1/\tau = \left(\alpha^2 + \beta^2 P^2\right)^{1/2} \tag{53}$$

where α, β, and γ are parameters which do not depend on pressure or frequency. Eliminating pressure from these expressions then leads, in terms of dimensionless quantities, to

$$\frac{1}{\omega_o\tau} = \left[\left(\frac{\alpha}{\omega_o}\right)^2 + \frac{(\beta/\omega_o)^2}{(\gamma/\omega_o)^4}\left(\frac{\omega_g}{\omega_o}\right)^4\right]^{1/2}. \tag{54}$$

The solid curves in Fig. 33 show Eq. (54) evaluated using the parameters appropriate for Samples 1 and 6 in argon gas. The region for optimum response is also indicated (Section 10). Sample 1 is the small-gap sample with the largest porosity, and Sample 6 is the large-gap sample with the smallest porosity. So none of our samples has optimum response.

The dotted curve shows the $1/\omega_o\tau$ values for Sample 1 scaled by 2.94. According to Eq. (49), this curve should correspond, for example, to a device identical to Sample 1 except for an increase in the number of 5 μm holes from 36 to $2.94 \times 36 = 106$. Similarly, the dashed curve which shows the scaling of the Sample 6 curve by a factor of 0.6, indicates the behavior of a device identical to Sample 6, but with 14, 3-μm holes instead of 24. Both scaled curves

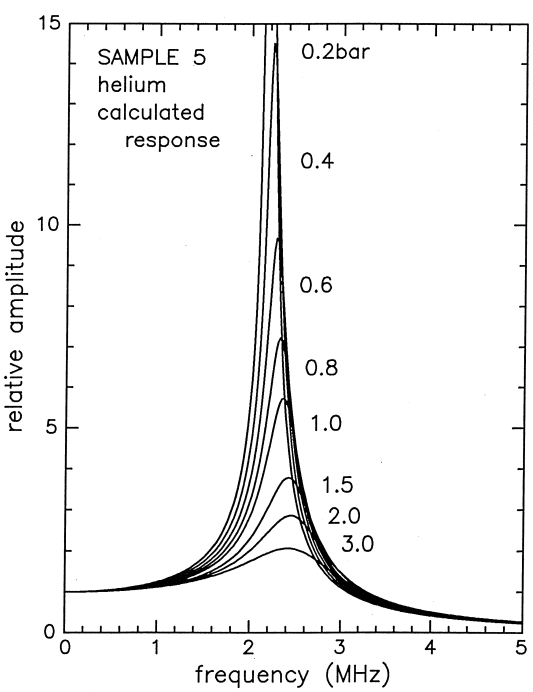

Fig. 30. Calculated resonance curves for Sample 5. These curves should be compared with the data shown in Fig. 16.

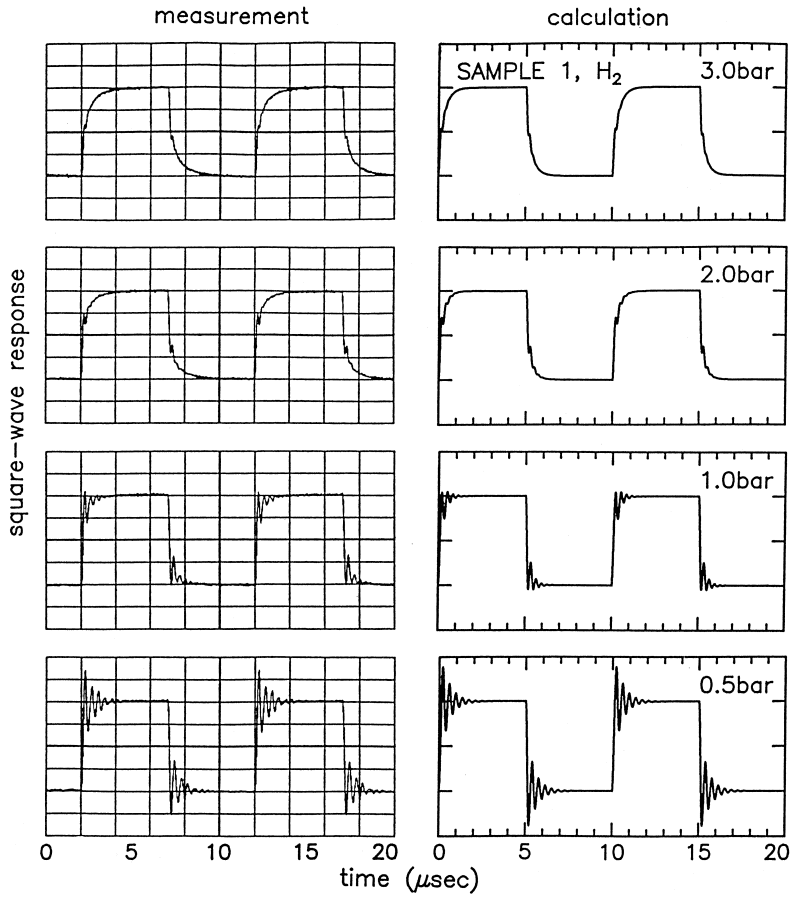

Fig. 31. Comparison of measured and calculated square-wave response for Sample 1 (small gap) in hydrogen.

generally run parallel to the optimized region, implying that a clean square-wave response can be achieved over a sizable range of gas pressures. Of course, the actual magnitudes of the gas pressures for these two devices are quite different. As a caution, it should be noted that 106 holes for the small-gap device corresponds to a density of holes much greater than actually studied and that at this density, Eq. (49) may underestimate the number of holes.

The pressure is determined using Eq. (7), which can be rewritten as

$$P = \left[\frac{\omega_g}{\omega_o} \Big/ \frac{\gamma}{\omega_o} \right]^2 . \tag{55}$$

In Section 11.3 above, it was determined that $f_g/P^{1/2}$ is 2.6 MHz/bar$^{-1/2}$ for the small-gap samples and 1.3 for the large-gap samples. Because $f_o = 2$ MHz, γ/ω_o is equal to 2.6/2 and 1.3/2, respectively. Using these numbers, and choosing to operate in the optimized region at $\omega_g/\omega_o = 2$, it follows that the corresponding pressures are 2.7 bars and 13.7 bars.

Fig. 34 shows a calculated set of response curves for the small-gap device with the optimized damping. Comparing these curves with those in Fig. 29, note that (1) the response at very low frequencies no longer falls rapidly below unity, (2) the frequency shifts are now much smaller, and (3) the response curve near 3 bars no longer shows any remnant of a resonance peak. The corresponding evolution in square-wave response is shown in Fig. 35, which can be compared with Fig. 31.

The evolution of square-wave response for the large-gap sample with 14, 3-μm (in diameter) damping holes is shown in Fig. 36. Note again the large pressure required to obtain a clean square-wave signal.

12. Modeling: an example

What is the fastest device that can be made with a gap of 0.97 μm if the ambient pressure is limited to a maximum of 2 bars? Assume first that the device diameter is kept at 150 μm.

Because the physical geometry is unchanged, f_g is still given by

$$f_g = 1.3P^{1/2} \tag{56}$$

and so, at a 2-bar pressure, $f_g = 1.87$ MHz. Insisting that $\omega_g/\omega_o \approx 2$, it follows that f_o must be 0.93 MHz, or roughly a factor of two smaller than the resonant frequency of the test devices.

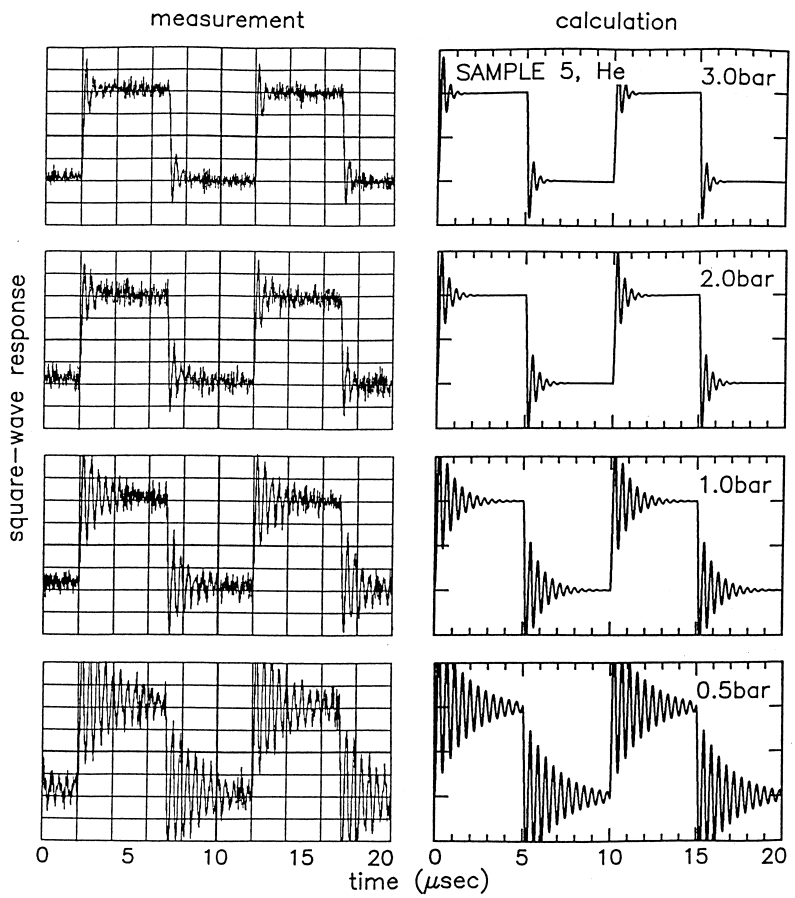

Fig. 32. Comparison of measured and calculated square-wave response for Sample 5 (large gap) in helium.

For a drumhead device,

$$f_o \sim \frac{1}{D}\sqrt{\frac{S}{\rho}}\,. \tag{57}$$

The natural frequency (with D fixed), therefore, can be decreased by a factor of two by decreasing the membrane

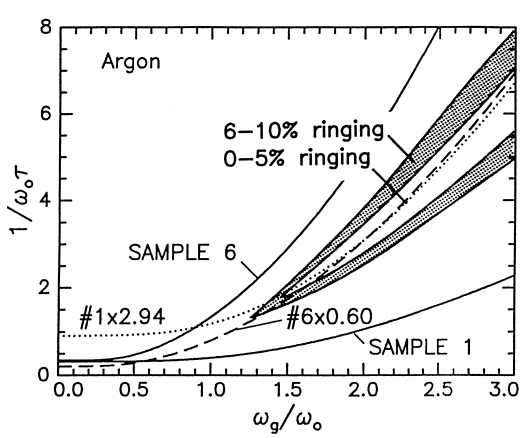

Fig. 33. $1/\omega_o\tau$ vs. ω_g/ω_o for Samples 1 and 6 in argon. The curve for Sample 1 (small gap) shows that more damping holes are required to achieve optimum square-wave response. The curve for Sample 6 (large gap) shows that fewer holes are required.

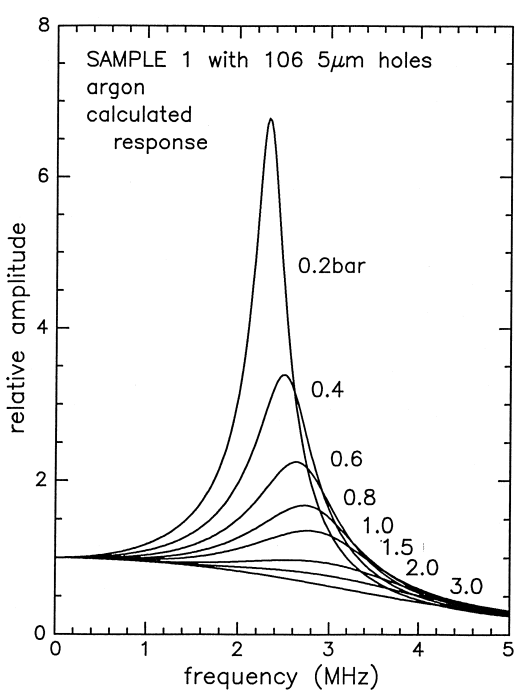

Fig. 34. Calculated response curves for a small-gap sample with the optimum arrangement of damping holes.

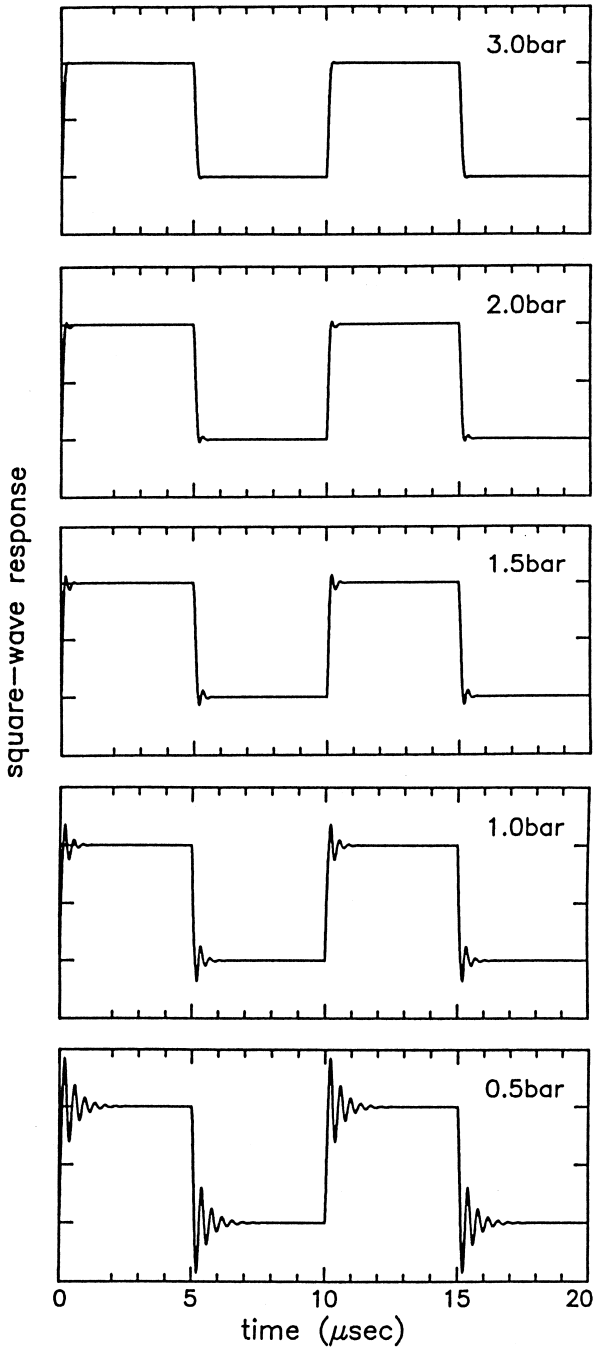

Fig. 35. Calculated square-wave response for a small-gap sample with the optimum arrangement of damping holes. Optimum response is achieved only for pressures greater than about 2 bars.

stress by a factor of four. The devices studied had a stress of about 800 MPa, so this would have to be reduced to roughly 200 MPa. One might also increase the average membrane density by increasing the thickness of the gold electrode.

Having chosen ω_g/ω_o to be 2, means from Fig. 13, that $1/\omega_o\tau$ must be about 3. Using $h = 0.97\ \mu m$, $D = 150$, $\omega_o = 0.93 \times 10^6 2\pi$, $P = 2$ bars, and the mass and viscosity for argon, Eq. (49) yields

$$1/\omega_o\tau = 0.023Nd, \tag{58}$$

which when set equal to 3 yields

$$Nd \approx 130\ \mu m. \tag{59}$$

If d is fixed at 5 μm, then $N = 26$; if N is fixed at 12, $d = 11\ \mu m$.

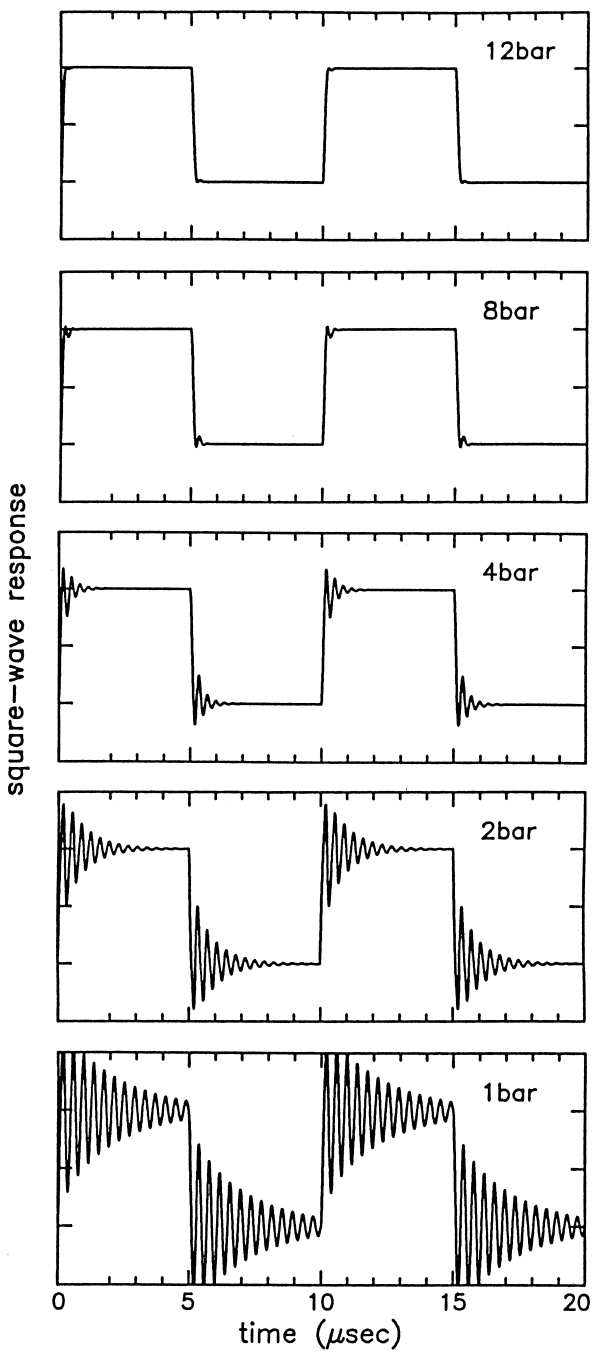

Fig. 36. Calculated square-wave response for a large-gap sample with the optimum arrangement of damping holes. Optimum response is achieved only for pressures greater than about 10 bars.

In the above sample calculation, D was taken to be 150 μm and S was altered to change the natural frequency. We now repeat the calculation with S fixed, allowing only D to vary.

Since f_g is independent of D, f_g continues to be given by Eq. (56), and f_o remains at 0.93 MHz. The natural frequency is now reduced to this value by increasing the drumhead diameter. Using Eq. (57), the diameter must be enlarged by the factor 2 MHz/0.93 MHz. The new diameter is then 322 μm. Eq. (49) now gives at $P = 2$ bars

$$1/\omega_o\tau = 0.0049Nd \tag{60}$$

which again is set equal to 3 to yield

$$Nd = 610. \tag{61}$$

One possibility is to have 122, 5-μm holes. Note that the density of 5-μm holes, N/D^2, is the same for both examples.

13. Summary

A simple phenomenological model was proposed to explain the gas-damping of squeeze-type micromachined devices. The physical model consists of a piston supported by a spring and located in a cylinder which is closed except for a number of small holes. These holes allow gas to enter or escape from the cylinder in response to the piston's displacement. With the assumption that the rate of gas flow is proportional to the pressure difference across the piston, the equations of motions were solved in terms of two reduced quantities ω_g/ω_o and $1/\omega_o\tau$. The main contribution to the damping was found to be due to the out-of-phase component of the cylinder pressure.

The region for optimum square-wave response, was mapped out in the $\omega_g/\omega_o - 1/\omega_o\tau$ plane and shown not to extend to the origin. One implication is that a minimum pressure must be exceeded to achieve optimum damping. This pressure is greater than atmospheric pressure for devices designed to operate above a few MHz, and rises quadratically with increasing frequency. Changing the pressure alone, however, cannot bring about optimum response, unless the effective piston porosity also has the proper magnitude.

By varying the values of the two model parameters, frequency and square-wave response curves were generated which exhibited the unusual features seen in some of the experimental data. In particular, frequency-response curves were obtained which showed a very rapid drop in frequency response near zero frequency, and square-wave response curves were obtained which clearly showed the effects of two very-different time constants.

Treating the two parameters as quantities to be determined empirically, the model was applied to a set of micromachined samples. Each of these devices was in the form of a cylindrical drum with a perforated drumhead membrane. The number and size of holes in the membrane varied as did the gap spacing between the membrane and substrate. Measurements were made using various gases and at several different gas pressures. Fits to each of the measured response curves were made to extract values of ω_g/ω_o and $1/\omega_o\tau$.

The ω_g/ω_o results were found to be independent of gas type and membrane porosity and in agreement with the expression derived for the piston model, namely:

$$\frac{\omega_g}{\omega_o} = \frac{P^{1/2}}{\omega_o\sqrt{ht\rho}}. \tag{62}$$

This agreement was interpreted as direct evidence for the applicability of the model to these particular structures.

The $1/\omega_o\tau$ values were found to be well-described by the simple purely-empirical relation

$$\frac{1}{\omega_o\tau} = 4.3\times10^9\frac{Ndh}{\omega_o D^2 M^{\frac{1}{4}}}\left[1+\frac{2.1M^{1/2}}{\eta}P^2\right]^{1/2}. \tag{63}$$

Acknowledgements

The authors have benefited greatly from interactions with Gary Boyd and Bernie Yurke.

References

[1] W.E. Langlois, Isothermal squeeze films, Quarterly Applied Mathematics XX (2) (1962) 131–150.
[2] W.S. Griffin, H.H. Richardson, S. Yamanami, A study of fluid squeeze-film damping, Journal of Basic Engineering (1966), pp. 451–456.
[3] J.J. Blech, On isothermal squeeze films, Journal of Lubrication Technology 105 (1983) 615–620.
[4] H. Seidel, H. Riedel, R. Kolbeck, G. Mück, W. Kupke, M. Königer, Capacitive silicon accelerometer with highly symmetrical design, Sensors and Actuators A 21–23 (1990) 312–315.
[5] J.B. Starr, Squeeze-film damping in solid-state accelerometers, Tech. Digest, IEEE Solid State Sensor and Actuator Workshop, Hilton Head Island, SC, June 1990, pp. 44–47.
[6] L. Zhang, D. Cho, H. Shiraishi, W. Trimmer, Squeeze film damping in microelectromechanical systems, ASME, DSC 40 (1992) 149–160.
[7] A. Beskok, G.E. Karniadakis, Simulation of slip-flows in complex micro-geometries, ASME, DSC 40 (1992) 355–370.
[8] M. Andrews, I. Harris, G. Turner, A comparison of squeeze-film theory with measurements on a microstructure, Sensors and Actuators A 36 (2) (1993) 79–87.
[9] E.S. Piekos, K.S. Breuer, DSMC modeling of micromechanical devices, AIAA-95-2089, 1995.
[10] T. Veijola, H. Kuisma, J. Lahdenperä, T. Ryhänen, Equivalent-circuit model of the squeezed gas film in a silicon accelerometer, Sensors and Actuators A 48 (1995) 239–248.

[11] Y.-J. Yang, S.D. Senturia, Numerical simulation of compressible squeezed-film damping, Solid-State Sensor and Actuator Workshop, Hilton Head Island, SC, June 3–6, 1996, pp. 76–78.
[12] C.L. Chen, J.J. Yao, Damping control of MEMs devices using structural design approach, Solid-State Sensor and Actuator Workshop, Hilton Head Island, SC, June 3–6, 1996, pp. 72–75.
[13] G.D. Boyd, D.S. Greywall, B. Yurke, Electromechanical Response of an Optical Modulator, unpublished.
[14] P.M. Morse, Vibration and Sound, 2nd edn., McGraw-Hill, New York, 1948, p. 397.
[15] S. Dushman, Scientific Foundations of Vacuum Technique, Wiley, NY, 1962.
[16] D.S. Greywall, Thermal-conductivity measurements in liquid ^{4}He below 0.7 K, Phys. Rev. B (1981), pp. 2152–2168.

Dennis Greywall received the BS degree in physics from the University of Detroit in 1965 and the PhD degree in low-temperature physics from Indiana University in 1970. Immediately thereafter, he joined Bell Laboratories in Murray Hill, New Jersey, as a member of technical staff. His work has included experimental studies at milliKelvin temperatures on single crystals of solid helium, on the various superfluid phases of liquid ^{3}He, and on the magnetic phases of two-dimensional ^{3}He. In 1993, he was awarded the London Prize in low-temperature physics. More recently, he has been involved in the design, modeling, and testing of MEMS devices.

Paul Busch is a member of the technical staff in the Physical Research Laboratory at Bell Laboratories in Murray Hill, New Jersey. He received the BS degree in physics from Upsala College in 1972. His work has included studies in condensed matter physics at ultra-low temperatures. Presently, he is involved in the mechanical testing of prototype MEMS devices.

James Walker is presently a Member of the Technical Staff in the Advanced Photonics Research Department at Lucent Technologies, Bell Laboratories, in Holmdel, New Jersey. His primary research interest is technology development for WDM telecommunications systems, with principle focus on MEMS components, such as the MARS data transmitter, MARS variable attenuator, and membrane-based WDM equalizer. He is also actively involved in research on high-speed CMOS interconnects using optical I/O and contributed to the development of the Opto-Electronic VLSI technology currently under investigation at Bell Laboratories. He was a member of the MEMS research group at Bell Laboratories from 1986 to 1990 and has contributed to a variety of MEMS research areas including thin-film shape memory alloys, material science of polysilicon, and friction and wear of micromechanical systems. He currently holds over 25 patents and has authored more than 35 published papers in the MEMS, Photonics, and packaging areas. He received the BS and MS degrees in electrical engineering from Rutgers University, in New Brunswick, New Jersey, in 1984 and 1989, respectively. He joined Bell Laboratories in 1984.